Integral measurements of plural and multiple scattering of electrons with energies between 10 and 100 keV for $6 \leq Z \leq 83$: I. Thin and intermediate-thickness targets

S. F. Barros[a,*], A. R. Petri[b,1], A. A. Malafronte[b], J. M. Fernández-Varea[c,b], N. L. Maidana[b], M. N. Martins[b], T. F. Silva[b], V. R. Vanin[b], A. Mangiarotti[b]

[a] *Instituto Federal de São Paulo, Campus Itaquaquecetuba, Rua Primeiro de Maio 500, Bairro Estação, CEP: 08571-050, Itaquaquecetuba, SP, Brazil*
[b] *Laboratório do Acelerador Linear, Instituto de Física, Universidade de São Paulo, Travessa R 187, Cidade Universitária, CEP: 05508-900, São Paulo, SP, Brazil*
[c] *Facultat de Física (FQA and ICC), Universitat de Barcelona, Diagonal 645, E-08028 Barcelona, Catalonia, Spain*

Abstract

Angle-integrated plural- and multiple-scattering distributions have been measured for electrons impinging with kinetic energies from 10 to 100 keV on targets with atomic numbers between those of C and Bi and mass thicknesses ranging from $\approx$ 5 to 300 μg/cm^2. The thinnest targets, $\approx$ 5 to 20 μg/cm^2, are not self-supporting and have been deposited on C backings with areal densities around 10 μg/cm^2. The intermediate-thickness ones are made of a single element and have mass thicknesses of $\approx$ 100 to 300 μg/cm^2. The electrons scattered at frontal angles are collected with a Faraday cup covering the polar angles below 12.0°. In addition, to supplement this information, an aluminium ring spanning a polar angle interval of 9.1° has been installed around the entrance of the Faraday cup and the charge deposited on it has also been recorded. The electrical current in the scattering chamber is measured as well so as to provide an accurate normalisation. Corrections for the fraction of impinging electrons backscattered by both the Faraday cup and the ring are applied to the data. The measurements are compared with the predictions of a Monte Carlo code that simulates each individual elastic collision. For targets made of a single element, the analytical Goudsmit–Saunderson and Lewis theories are tested as well. In all cases, the single-scattering angular differential cross sections, obtained by partial-wave solution of the Dirac equation in a self-consistent central potential, are taken from the ICRU Report 77. Good agreement is found within the uncertainties of the data. An analytical formula for the angular integration of the Goudsmit–Saunderson distribution is presented in an Appendix.

Keywords:
Plural scattering, multiple scattering, Goudsmit–Saunderson theory, Lewis theory

1. Introduction

Electron multiple scattering (MS) in matter is an old and venerable subject, essentially started by Sir J. J. Thomson himself as a way to confirm his atomic model (Thomson, 1910). Shortly afterwards, measurements of the transmission coefficient of β-rays through thin films were employed by Crowther (1910) to probe the distribution of the positive charge and the number of electrons in the atom. Theoretical development was relatively fast and the analytical approaches used up to the present days were introduced by Goudsmit and Saunderson (1940a,b). Their formulation does not take into account secondary electrons, energy loss, or correlations between the number of collisions and the deflection angle. So it is essentially applicable to thin targets and away from the angular regions where target finite-size effects (resulting in a higher probability of interaction) are important. The energy loss was later incorporated to the Goudsmit–Saunderson approach by Lewis (1950) in the continuous-slowing-down approximation (CSDA), thus assuming a one-to-one correspondence of energy with path length and implicitly excluding situations where energy-loss straggling is important. Secondary electrons and those stopped inside the target are again disregarded, thus limiting the applicability to thicknesses well below the CSDA range and to angles where target finite-size effects are not important. The strongest advantage of the Goudsmit–Saunderson formulation is that an arbitrary single-scattering elastic differential cross section (DCS) can be supplied as input. However, the simplified theory by Molière (1947) became more popular in the past because it gives the result in terms of universal functions that can be tabulated once and for all (Andreo et al., 1993), of course at the price of simplifying assumptions (Fernández-Varea et al., 1993). Only with the advent of digital computers, it was possible to routinely apply the Goudsmit–Saunderson or Lewis theories to state-of-the-art elastic DCSs obtained from a partial-wave solution of the Dirac equation for realistic self-consistent atomic fields. One notable effort of such a type being the database of elastic DCSs and MS programs made publicly available with the ICRU Report 77 (Berger et al., 2007).

Monte Carlo (MC) tools may seem particularly adequate for treating MS offering the possibility to include naturally secondary electrons, energy loss, and target finite-size ef-

*Corresponding author: Tel.: +55 1198614-1607; fax: +55 98614-1607.
Email address: suelen.barros@ifsp.edu.br (S. F. Barros)
[1] Current address: INFN, Sez. Milano.

fects (Shimizu and Ze-Jun, 1992); but their practical use has encountered the difficulty that electron elastic DCSs are large: typical elastic mean free paths span from 1 nm to 1 μm for energies varying between 10 and 100 keV, respectively. This has led to the introduction of ever more refined methods in modern MC codes (Berger, 1963, Kawrakow and Bielajew, 1998), most notably the so-called "random hinge" implemented in the PENELOPE code (Fernández-Varea et al., 1993). The widely-used Geant 4 package has a MS model that relies on random sampling from large tables precalculated with the Goudsmit–Saunderson theory (Kadri et al., 2009).

The continuous attempts to improve the theoretical description of MS have not been matched on the experimental side. Despite our best efforts to search the available literature for MS data in the energy range from 10 to 100 keV, we found only two such publications by Dees and Hamermesh (1943) and by Cosslett and Thomas (1964a). The situation is not much better for elastic scattering DCSs, as it can be seen from the validation section of the ICRU Report 77 (Berger et al., 2007) or the comparison from eV to GeV by Haque et al. (2018). Such a state of affairs should not be confused with that of transmission or backscattering coefficients, for which ample literature (Cosslett and Thomas, 1965, Neubert and Rogaschewski, 1980) and even databases (Joy, 1995) do exist. Measurements of very forward angular distributions (below 10^{-2} rad) have also been made (Marton et al., 1962, Cosslett and Thomas, 1964b, Swanson and Powell, 1966) because they were important for the development of electron microscopy or to study the excitation of plasmons.

In this context, we decided to undertake an effort to provide MS data in the 10–100 keV energy interval, first integrated ones, taking advantage of the already developed setup (Martins et al., 2022). Differential ones with a new detection system (Malafronte et al., 2021, Mangiarotti et al., 2021b) will follow in the future. Several targets of different elements and mass thicknesses have been measured, ranging from thin ones ($\approx$ 5 to 20 μg/cm^2), which are not self-supporting except for the C backing alone, to intermediate self-supporting ones ($\approx$ 100 μg/cm^2) and, finally, thick ones ($\approx$ 2 mg/cm^2). From the brief mention of available theories given above, it is clear that only homogeneous targets from the first two classes can be compared meaningfully to the Goudsmit–Saunderson and Lewis formulations. Thus, we decided to avoid overloading the present article with too many figures and include only the data for thin and intermediate targets in the present part I. Those for the thick ones have already been measured in the same runs for overall consistency, but will be discussed in the subsequent part II (Barros et al., 2022a); they are mostly useful to validate MS approaches in general-purpose MC codes like PENELOPE. The present MS data are made available with their uncertainties in tabular form in the supplementary material.

This paper is organised as follows. The experimental setup is presented in Sec. 2, discussing, in particular, how the thicknesses of the targets have been determined (Sec. 2.1), the details of the chamber (Sec. 2.2), and of the measurement procedure (Sec. 2.3). The available theories are summarised in Sec. 3 giving enough details to understand the issues raised by the comparison with data. A simple in-house MC program (Sec. 4) simulating explicitly each elastic collision, has been used to compare with the measurements, but especially to allow the propagation of the uncertainties. The data analysis procedure is described in Sec. 5, explaining the test that is performed to discover possible changes in the beam conditions with time (Sec. 5.1), the corrections applied (Sec. 5.2) and, finally, how all the uncertainties are propagated and combined together (Sec. 5.3). The final results are presented and discussed in Sec. 6 and the conclusions offered in Sec. 7. Some technical details on an analytical integration method of the Goudsmit–Saunderson angular distributions are addressed in AppendixA.

2. Experiment

Integral measurements of MS angular distributions have been made with a monoenergetic and well-collimated electron beam using a setup installed at the dedicated low-energy line of the São Paulo Microtron. The scattered electrons have been collected by two devices: one is a graphite Faraday cup, covering the most forward angles, and the other is a ring-shaped aluminium electrode that surrounds the entrance of the Faraday cup and covers larger polar angles still in the forward direction. The arrangement is similar to that employed in previous experiments on electron-atom interactions (Barros et al., 2018, García-Alvarez et al., 2018, Santos et al., 2019), and it is described at length by Vanin et al. (2019). Further improvements, specifically implemented for the present study, have been made and are reported by Martins et al. (2022). We provide below a description of the set-up with enough details to understand how the data are analysed; the reader interested in more information is directed to the above publications. The targets irradiated for the present part I have been fabricated employing elements of atomic numbers Z between 6 and 83, with mass thicknesses ranging from $\approx$ 5 to 300 μg/cm^2. A series of thicker targets has also been measured but, as mentioned, the results, mostly useful to validate MC simulations, will be presented in part II.

2.1. Target preparation and characterisation

The targets employed in the current experiment are, as anticipated above, of two types: the thin ones, with mass thicknesses smaller than $\approx$ 20 μg/cm^2, and the intermediates ones, with mass thicknesses $\approx$ 100–300 μg/cm^2. The former are actually too fragile unless deposited on a backing made by a thin C film (we indicate explicitly its presence in the target name to remind the reader that it must be accounted for when comparisons with simulations are made, like in Sec. 6). To be specific, those with a C backing are: Al/C, Cu/C, Te/C, Au/C, and Bi_2O_3/C; and the intermediate ones are Al, Cu, and Au.

The thin Cu/C target has been prepared by magnetron sputtering, while the other thin and intermediate ones have been manufactured by physical vapour deposition (Vanin et al., 2019). The C backings have also been prepared by evaporation and their thicknesses are between 10 and 60 nm, which has proven adequate to provide mechanical stability. All targets are mounted on rectangular frames made of C fibre with dimensions of 15 mm$\times$30 mm and a thickness of 0.3 mm. The frames

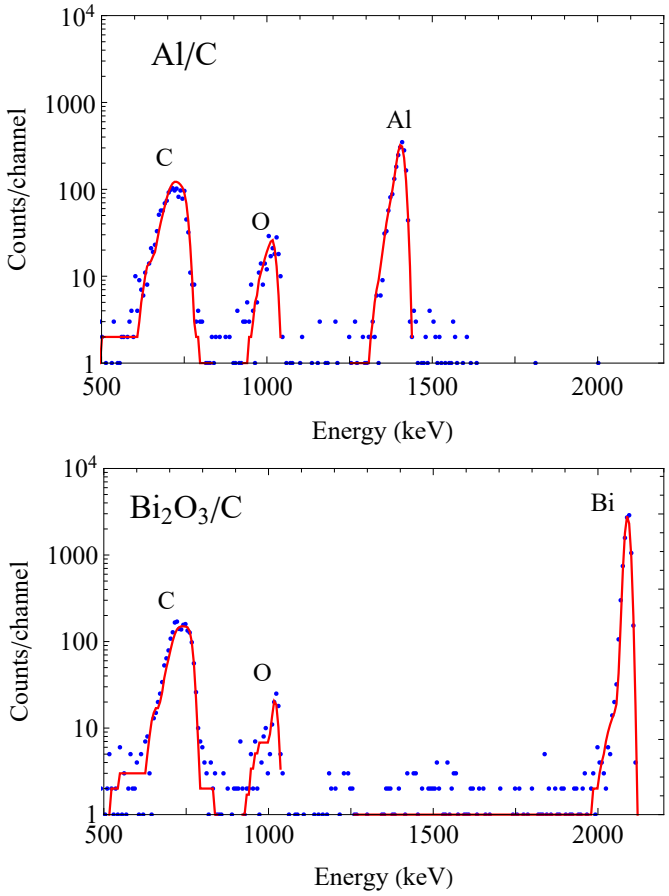

Figure 1: Rutherford backscattering spectra of 2200(11) keV $^4He^+$ ions incident on the Al/C (upper panel) and Bi_2O_3/C (lower panel) targets. The dots are the experimental values and the curves are the MultiSIMNRA simulated spectra. The energy dispersions are 5.9 and 6.4 keV/channel for the Al/C and the Bi_2O_3/C targets, respectively.

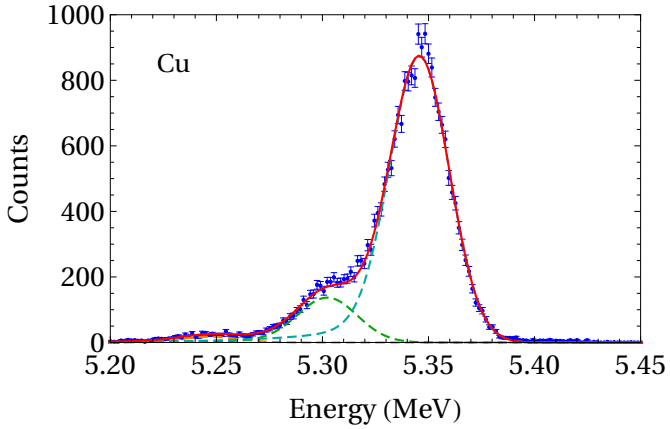

Figure 2: Energy spectrum of the α-particles emitted by ^{241}Am after passing through the Cu intermediate target. The data are the dots with the uncertainty bars (representing 1 standard deviation). A simultaneous fit (continuous curve) is performed modelling each of the three peaks (dashed curves) with the detector response function described in the text. The energy dispersion is 1.6 keV/channel.

have a laser-cut 10-mm circular hole to expose the target to the beam.

Three methods have been employed to characterise the targets, aiming at a compromise between the best accuracy and practical considerations. In particular, the targets are very fragile and approximately 20% are broken during installation or removal. The chances to survive two experimental campaigns is thus small. Whenever possible, it has been avoided.

For the targets with backing (Al/C, Cu/C, Te/C, Au/C, and Bi_2O_3/C) as well as the Au intermediate one, the areal densities have been determined by Rutherford backscattering spectrometry (RBS) of $^4He^+$ ions. This technique is the only one capable of dealing with targets composed of layers. The measurements have been conducted at the LAMFI laboratory of the University of São Paulo (Brazil) employing a Pelletron tandem accelerator. The impinging energy has been set to 2200(11) keV. The energy spectra of the backscattered particles have been recorded with a surface barrier Si detector, placed at 120.0(5)° with respect to the direction of the incident ions. The beam current has been kept at $\approx$ 10 nA and the data acquired until the integrated charge reached 10.0 μC. Two typical spectra, for the Al/C and Bi_2O_3/C targets, are shown in Fig. 1. To extract the areal density of the C backing and the material deposited on it, a calculated spectrum is fitted to the data employing MultiSIMNRA (Silva et al., 2016), a standard simulation tool for RBS. The final results, obtained after the procedure has converged, are also reproduced in Fig. 1. As a by-product, it is also possible to quantify the presence of other elements, most commonly due to oxidation of the deposit, as it is clearly visible the case of Al in Fig. 1. Such a process is important only for the thin targets and the oxygen content is given in Table 1. However, the MS calculations described in Sec. 6 will show that, within the present combined experimental uncertainties, the inclusion of oxygen is not necessary. No oxygen has been detected by RBS in the intermediate Au target. More details on the experimental set-up as well as on the estimates of the sources of uncertainty on the areal densities determined with this procedure can be found elsewhere (Santos et al., 2019).

The areal densities (number of atoms or molecules per unit surface) of the Al and Cu intermediate targets (which are self-supporting) have been determined relying on the energy lost by α-particles emitted from a ^{241}Am radioactive source. These measurements were already performed on a series of targets as a left-over from another experiment (Mangiarotti et al., 2021a). An open deposit with a small thickness of active material has been selected to avoid energy loss and energy-loss straggling of the α-particles in the source itself. The energy spectra of the α-particles, before and after passing through the target, have been measured with a Si barrier detector. As an example, the case of the self-supporting Cu target is displayed in Fig. 2. The three peaks from ^{241}Am (with very different intensities) are clearly separated. Only the highest energy (5.48556 MeV) and most intense one (corresponding to a yield of 85%) is used to determine the energy lost by the α-particles because it gives the best accuracy. However, due to the partial overlap produced by the finite resolution of the detector and the energy-loss straggling, the three peaks are considered simultaneously in the fit, see again Fig. 2. The asymmetric response of the detector is

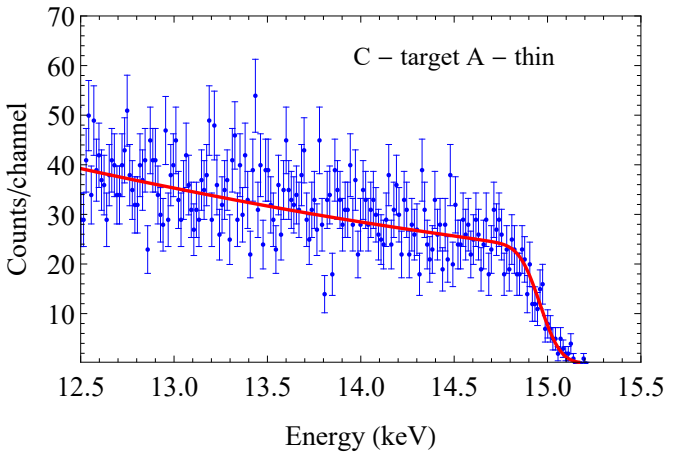

Figure 3: Photon energy spectrum obtained with 14.94-keV electrons impinging on the C target A. The points with the uncertainty bars (representing 1 standard deviation) denote the data and the red curve the theoretical model described in the text for the fitted parameters. The energy dispersion is 14 eV/channel.

modelled adopting the convolution of a Dirac δ-function plus a one-side exponential with a Gaussian (L'Hoir, 1984). A good energy calibration is obtained by including a ^{232}Th source with all its daughters, spanning the energy range from 8.78517 MeV (^{212}Po) to 3.9485 MeV (^{232}Th). For a good accuracy, it is important to cover the final energy of the α-particles exiting the target. Note that only the slope of the calibration curve (gain) enters into the determination of the target thickness. Finally, reliable stopping power tables are necessary. To obtain the areal densities of the manufactured targets, the compilation contained in the ICRU Report 49 (Berger et al., 1993), also available as part of the NIST Standard Reference Database Number 124 (Berger et al., 2017), has been chosen. As a matter of fact, the ICRU Report 49 values, as well as the setup and programs, have been tested using the Al and Cu targets of part II (Barros et al., 2022a), which are thick enough to have the results confirmed by direct measurement of their weight and area. The differences are well within the uncertainty of the calibration targets of 0.5%, which is our conservative estimate of the overall accuracy.

For the two C targets, a procedure that relies on the intensity of the bremsstrahlung spectrum has been applied following Fernández-Varea et al. (2014) to avoid a second installation in a different setup. To such end, an analytical model is built from the convolution of the detector response function, taking into account its full-energy peak efficiency, with the bremsstrahlung DCSs tabulated by Seltzer and Berger (1986), Kissel et al. (1983), and the energy distribution of the electron beam, assumed to have a Gaussian shape. The free parameters are: the average and the width of the beam energy distribution; and a parameter that is proportional to the product of the areal density of the target with the total incident charge. Measuring the latter during irradiation, it is possible to obtain an estimate of the former. The model has been used to describe the highest-energy region of the photon spectrum (tip) acquired with a solid-state detector (see Sec. 2.2). Such a choice ensures that only single bremsstrahlung emissions dominate the measured yields. Figure 3 depicts the tip of the bremsstrahlung spectrum measured with the C target A when irradiated with a 14.94-keV electron beam using the photon detector described in the next section. The continuous curve is the result of the described model, when calculated with the parameters obtained from the fit. Five values of the areal density are available considering the beam energies where the photon detector has a good efficiency (i.e. 12.77, 14.94, 16.85, 18.80, and 20.69 keV). The best estimate of the areal density is given by the average. The standard deviation of the five determinations is $\approx 2\%$.

The uncertainties of this third methodology (determined by adding quadratically the $\approx 2\%$ mentioned above to the uncertainties of the method, namely: determination of the efficiency of the detector, charge measurement, and bremsstrahlung cross section) are of the order of 10%, dominated by the limitations on the knowledge of the bremsstrahlung DCSs tabulated by Seltzer and Berger (1986), Kissel et al. (1983). Because of this large value, when compared to that of the other methods employed here, two different C targets have been irradiated to allow a mutual cross check of the consistency of the results.

The areal densities of the manufactured targets are collected in Table 1 together with their estimated uncertainties (given as 1 standard deviation).

2.2. *Scattering chamber and detection system*

The scattering chamber is a hollow cylinder, with an internal diameter of 490 mm, made of stainless steel. The upper and

Table 1: Areal densities of the targets employed in the present work, together with their uncertainties (1 standard deviation). The units are atoms/cm^2, except for Bi_2O_3, where they are molecules/cm^2. Moreover, for the Bi_2O_3/C target, the measured quantity of oxygen is, within the uncertainties, well compatible with being all bound in the molecule. Therefore, we assume that no free oxygen is present and fix its content accordingly to the measured quantity of bismuth, which is known with much better precision, see Fig. 1. For the other thin targets, the areal densities of the oxygen contamination (when detected) and the C backing are given separately to be accounted for in the simulations (see Sec. 6). A sulphur contamination of $1.3(3) \cdot 10^{16}$ atoms/cm^2 has only been found by RBS for the Cu/C case.

Target	Element (atoms/cm^2)	Oxygen (atoms/cm^2)	C backing (atoms/cm^2)
	Thin targets		
C, target A	$4.7(6) \cdot 10^{17}$	-	-
C, target B	$5.3(7) \cdot 10^{17}$	-	-
Al/C	$1.40(9) \cdot 10^{17}$	$4.0(7) \cdot 10^{16}$	$5.7(3) \cdot 10^{17}$
Cu/C	$1.58(7) \cdot 10^{17}$	$4.9(7) \cdot 10^{16}$	$5.1(5) \cdot 10^{17}$
Te/C	$9.6(4) \cdot 10^{16}$	$1.0(2) \cdot 10^{16}$	$4.8(2) \cdot 10^{17}$
Au/C	$1.35(11) \cdot 10^{16}$	$3.4(8) \cdot 10^{15}$	$1.29(16) \cdot 10^{17}$
Bi_2O_3/C	$7.9(4) \cdot 10^{15}$	-	$6.5(6) \cdot 10^{17}$
	Intermediate targets		
Al	$2.80(2) \cdot 10^{18}$	-	-
Cu	$3.27(3) \cdot 10^{18}$	-	-
Au	$3.70(15) \cdot 10^{17}$	-	-

lower covers are thick aluminium discs (Vanin et al., 2019). At zero degrees with respect to the beam line, the scattering chamber is equipped with a Faraday cup made of graphite, see the upper panel of Fig. 4. Its shape is a truncated cone with an opening angle of $\Theta_{FC} = 12.0(5)^\circ$. The vertex of the cone is designed to correspond to the nominal position where the beam hits the target. The Faraday cup is 195 mm deep and it has an internal diameter of 200 mm at the bottom, 10-mm-thick lateral walls, and a 20-mm-thick bottom. The graphite cup is mounted inside a support, also with the same shape of a truncated cone and made of stainless steel, fixed to the chamber. A graphite ring has been added to surround the entrance of the Faraday cup and screen the rim of the latter from electrons scattered by the target. This ring covers an angular aperture $\Delta\Theta = 11.1(5)^\circ$, from 12.0° to 23.1°. The graphite cup and ring are mounted in such a way that they remain electrically insulated from each other and from the chamber. They are connected to feedthroughs so that the charge they collect can be measured. The chamber itself is also mounted in such a way that it remains insulated from mechanical supports, beam line, and vacuum pump, making it possible to measure the charge it collects. All the three structures together provide a quite accurate determination of the total charge impinging on the target, used for absolute determination of the cross sections in previous publications (García-Alvarez et al., 2018, Santos et al., 2019, Barros et al., 2022b). The ratio of the current collected by the Faraday cup and the ring over the total provides a rather sensitive monitoring of systematic drifts of the beam spot from its focused position on the target (see Sec. 2.3).

However, previous studies, described in more depth by Martins et al. (2022), have shown that some electrons, which are backscattered by the walls of the Faraday cup and are able to return into the chamber, can also hit the graphite ring on the back. Since this is an unwanted effect both from the point of view of monitoring the drift of the beam position and the integrated MS measurements of the present work, a second ring, made of aluminium, has been installed in front of the graphite ring in such a way that it remains insulated (Martins et al., 2022). This second ring is smaller and has an angular aperture $\Delta\Theta' = 9.1(5)^\circ$, from $\Theta_{R_i} = 14.4(5)^\circ$ to $\Theta_{R_o} = 23.5(5)^\circ$ so that the electrons backscattered by the Faraday cup cannot reach it. The graphite ring is then electrically connected to the chamber and only the charge collected by the aluminium one is measured. A drawing of these two rings (graphite and aluminium) is displayed in the lower panel of Fig. 4.

A two-ring system, mounted on a movable support, has also been manufactured after the successful operation of the fixed one (Martins et al., 2022). It has been employed to study the fraction of electrons that is backscattered from the target, hit the walls of the chamber, and is backscattered once more in the frontal direction reaching the Faraday cup and the fixed aluminium ring. This is an important source of target-generated background for thick targets with high-Z and it is necessary to subtract it, as discussed in more details in part II. It is not important in the case of concern here of thin and intermediate targets, see again part II.

The electrical charges collected by the Faraday cup, the aluminium ring, and the scattering chamber are measured with three Digital Current Integrators, model 439 by Ortec (Glass et al., 1967). Their design is optimised to achieve very low input parasitic currents and no integration dead time. The time stability is excellent (below 0.05%, if allowed to warm-up for half an hour before starting the measurements (Martins et al., 2022), as we have always done). The output pulses are counted on a custom-made multichannel scaler, which outputs histograms with 1 s bins. Therefore, a statistical analysis of possible time drifts can be undertaken as described in Sec. 5. When the Ortec 439 is directly connected to a picoampere current source model 261 by Keithley, the observed deviations from a linear response are well compatible with the stated accuracies (0.3% for the Ortec 439 with a setting of 10^{-10} Coulomb/pulse for the current range employed in the present work and 0.25% for the picosource). However, when the electrical properties of the combined system (collecting electrode, cable, and charge integrator) are studied, the conclusions are different (see Sec. 4 in the article by Martins et al. (2022)). In particular, a loss of charge is present ranging from ≈ 3–2% for currents of ≈ 100 *nA* decreasing to 0.5% at ≈ 500 to 1000 nA. The worst cases belong

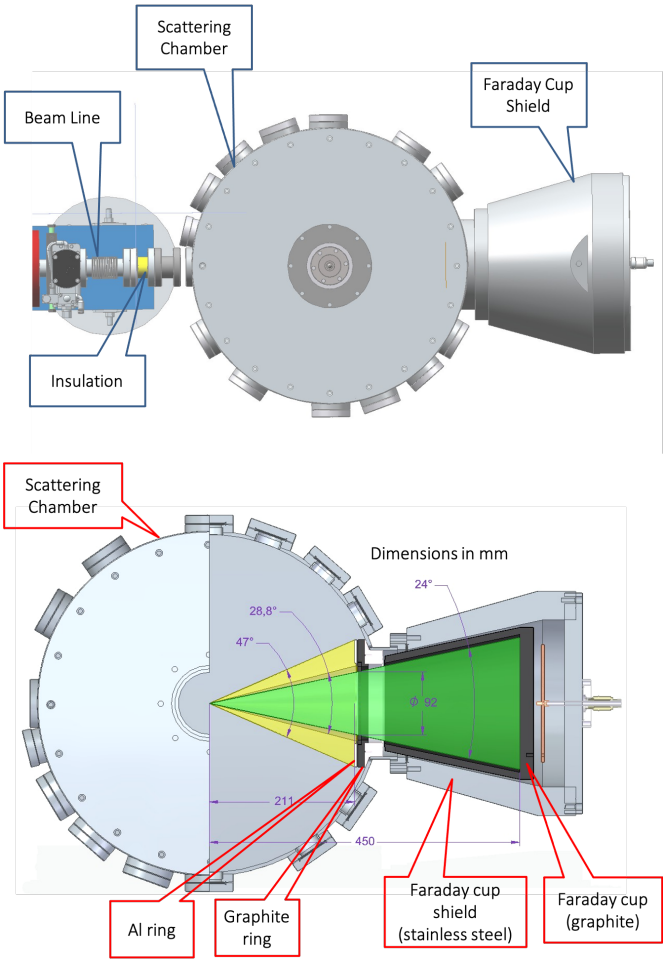

Figure 4: Drawings of the scattering chamber and Faraday cup. The complete system and the inner structure of the chamber and Faraday cup are shown (upper and lower panels). The ring is visible only in the lower panel. The values of $2\,\Theta_{FC}$, $2\,\Theta_{R_i}$, and $2\,\Theta_{R_o}$ are also indicated.

to the chamber, being a large macroscopic object, whose insulation is more difficult (see Fig. 6 by Martins et al. (2022)). A third degree polynomial (whose constant coefficient is zero) has been fitted to the counts-versus-current curves independently for each Ortec 439 module and used to determine the collected charge (Martins et al., 2022) correcting for such losses.

The quantities accessible with the present setup are the ratios

$$R_{\mathrm{FC}} \equiv \frac{Q_{\mathrm{FC}}}{Q_{\mathrm{FC}} + Q_{\mathrm{R}} + Q_{\mathrm{C}}} \ , \qquad R_{\mathrm{R}} \equiv \frac{Q_{\mathrm{R}}}{Q_{\mathrm{FC}} + Q_{\mathrm{R}} + Q_{\mathrm{C}}} \ , \qquad R_{\mathrm{C}} \equiv \frac{Q_{\mathrm{C}}}{Q_{\mathrm{FC}} + Q_{\mathrm{R}} + Q_{\mathrm{C}}} \ , \tag{1}$$

where Q_{FC}, Q_{R}, and Q_{C} are the charges collected by the Faraday cup, the ring, and the chamber, respectively. Note that only two amongst R_{FC}, R_{R}, and R_{C} are independent, owing to the constraint $R_{\mathrm{FC}} + R_{\mathrm{R}} + R_{\mathrm{C}} = 1$. The values of R_{FC} and R_{R} are given, in terms of the MS probability density function (PDF) per unit solid angle $p_{\mathrm{MS}}(\Theta)$, as

$$R_{\mathrm{FC}} = 2\pi \int_{\cos\Theta_{\mathrm{FC}}}^{+1} p_{\mathrm{MS}}(\Theta)\, \mathrm{d}(\cos\Theta) \ , \qquad R_{\mathrm{R}} = 2\pi \int_{\cos\Theta_{\mathrm{R_o}}}^{\cos\Theta_{\mathrm{R_i}}} p_{\mathrm{MS}}(\Theta)\, \mathrm{d}(\cos\Theta) \ . \tag{2}$$

Thus, with the present method, only integral measurements of p_{MS} are possible. No dependence on the azimuthal angle is expected for homogeneous beams and targets with the setup geometry. Moreover, Eqs. (2) are strictly valid under the assumption that all electrons impinging on the Faraday cup or the ring are retained without any loss due to backscattering. This is not realistic and corrections have to be applied (see Section 5.2). The experience with voltages applied to the collecting structures has not been encouraging (Martins et al., 2022). Therefore, no bias is connected, resulting in no selection on the energy of the electrons and no suppression of secondary electrons possibly leaving the electrodes.

The scattering chamber has also a special device to hold the targets, called ladder in the following. The ladder is connected, through vacuum-proof bellows, to a remotely-controlled linear actuator mounted on the top cover. This allows to exchange the target by means of vertical translations without breaking the vacuum. Six slots are available, while a BeO viewscreen is permanently installed. As a matter of fact, it is possible to tune the beam position and size by observing remotely with a camera its fluorescence image. Finally, the linear actuator can make a large enough translation to actually remove all materials from the beam, which can then pass freely and reach the Faraday cup without interacting.

A Silicon Drift Detector (SDD, model X-123SDD by Amptek®) is installed in such a way that its support structure penetrates through a vacuum-tight o-ring and holds the active element inside the chamber. It is located at 48.9° with respect

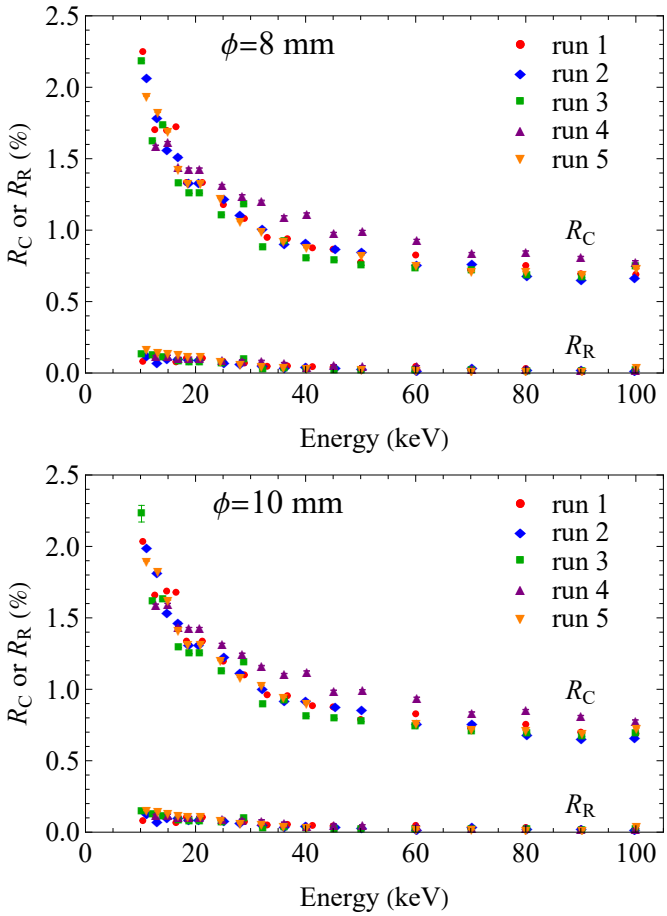

Figure 5: Ratios R_{C} and R_{R}, see Eqs. (1), when electrons in the energy range from 10 to 100 keV are focused at the centre of the hollow frames with diameters of 8 mm (upper panel) and 10 mm (lower panel).

to the incident beam direction and has been employed to measure the photon spectrum during all irradiations. The ladder slots have been filled, for all irradiations, in such a way that one target has always been a thin one. So, at least in this particular case, it is possible to apply the model presented in Sec. 2.1 to describe the highest-energy region of the bremsstrahlung spectrum for all runs below 40 keV. The fit then gives the energy of the incident beam with an accuracy of ≈ 50 eV. Above 40 keV, the detector efficiency drops considerably and the application of the procedure becomes impractical. The beam energy is then obtained by reading the accelerating potential with a voltmeter, the accuracy being somewhat worse ≈ 500 eV.

2.3. *Measurement procedure*

The irradiations have been performed at eighteen energies in the interval from 10 to 100 keV. They have been organized into five runs. In each of them, the target ladder has been filled with at least one thin target, one intermediate, and two hollow frames. The beam current has been set between 200 and 900 nA, so that irradiation times varied from 300 to 600 s. The pressure inside the vacuum chamber has been kept at about $7 \cdot 10^{-5}$ Pa during all the measurements.

During the irradiations, each target has been positioned at the centre of the scattering chamber, perpendicular to the direction of the incident beam. The tuning of the beam position and its focusing are the most delicate parts of the experiment because they can directly affect the sharing of the charge between the Faraday cup and the ring. To confirm that the beam has been properly set, the two hollow frames, with internal diameters of 8 and 10 mm, have been employed. The electron beam has been passed through their centre and then $R_{\rm FC}$ and $R_{\rm R}$, see Eqs. (1), have been evaluated. If $R_{\rm FC}$ and $R_{\rm R}$ are approximately the same in the two cases, implying that the electron beam is not grazing the holes, the settings are considered correct and the irradiation of the actual targets is carried out. On the other hand, if a difference between these ratios is found, the beam is refocused and the confirmation with the frames is redone. Note that since the beam optics depends on the energy of the beam, the focusing and the check described must be repeated each time the energy is changed.

In addition to enabling the verification of beam focusing, the value of $R_{\rm C}$, obtained when the beam is well focused at the centre of each of the two hollow targets, also furnishes an estimate of the charge fraction $f_{\rm FC}$ that reaches the Faraday cup and is backscattered from it to the chamber. Figure 5 shows $f_{\rm FC} \equiv R_{\rm C}$ and $R_{\rm R}$, after proper focusing has been reached, at the various energies used in all the five runs. The values of $f_{\rm FC}$ drop from around 2% to 0.7%, when the electron energy increases from 10 to 100 keV. Fig. 5 is in overall agreement with previous experiments, as well as MC simulations performed to evaluate the Faraday cup geometry (Vanin et al., 2019). However, older measurements of $R_{\rm R}$ for hollow frames referred to the graphite ring, the aluminium one being installed for this experiment, as mentioned in Sec. 2.2. Hence, those results cannot be exactly compared with the present ones.

3. Available theories

One of the best analytical theories of MS was developed by Goudsmit and Saunderson (1940a,b). It is based on two main assumptions: a) the elastic DCS is constant and b) the number of collisions fluctuates according to a Poissonian, whose mean value is the ratio of the path length s to the elastic mean free path λ. The analytical formulae, which can be found e.g. in the ICRU Report 77 (Berger et al., 2007) or in the publications by Fernández-Varea et al. (1993) and Negreanu et al. (2005), are based on an expansion of the single-scattering elastic DCS in terms of Legendre polynomials

$$\tilde{\lambda}_\ell^{-1} \equiv (\lambda_\ell/\lambda)^{-1} \equiv 2\pi \int_{-1}^{1} \left[1 - P_\ell(\cos\theta)\right] p_{\rm SS}(\theta)\, {\rm d}(\cos\theta) \ , \quad (3)$$

where P_ℓ is the Legendre polynomial of order ℓ, the elastic mean free path is $\lambda = 1/(\mathcal{N}\sigma)$ (being σ the total (i.e. integrated) elastic cross section and $\mathcal{N}$ the number density of the target), and, finally, $p_{\rm SS}(\theta)$ the PDF of an angular deflection into the solid angle $2\pi\,{\rm d}(\cos\theta)$ for a single scattering (i.e. $\sigma\, p_{\rm SS}(\theta)$ is the elastic DCS). The angles of the electron momentum, relative to the impinging beam direction and the direction before the collision, are referred as Θ and θ, respectively, being, in general, different due to MS. The quantity λ_ℓ that appears in Eq. (3) is the ℓ-th transport mean free path (Fernández-Varea et al., 1993). The convolution of $p_{\rm SS}(\theta)$ with itself n times, representing the effect of n collisions, can then be evaluated as a closed formula, given the azimuthal symmetry of the problem. Finally, this general form of the n-th convolution is weighted with a Poissonian giving a final result which is expressed as a sum over all Legendre polynomials used in the expansion of the DCS

$$p_{\rm GS}(\Theta; s) \equiv \sum_{\ell=0}^{\infty} \frac{2\ell+1}{4\pi}\, \exp(-\langle n\rangle/\tilde{\lambda}_\ell)\, P_\ell(\cos\Theta) \ , \quad (4)$$

which represents the PDF of an angular deflection in the solid angle $2\pi\,{\rm d}(\cos\Theta)$ after crossing a path length s, where the average number of collisions is $\langle n\rangle = s/\lambda$. The Goudsmit–Saunderson formulation is actually a specific example of a compound Poisson stochastic process (Ning et al., 1995).

The convergence of Eq. (4) is somewhat peculiar: for a rather thick path lengths, the electrons suffer many collisions and the angular distribution is isotropic: it can be described by the first term ($\ell = 0$) alone. On the contrary, the angular distribution from rather thin path lengths, where very few interactions can happen and may appear the simplest case, requires a very large number of terms to be represented accurately. The sharper the angular distribution, the more Legendre polynomials are needed to represent it. Berger and Wang (1988) noted that the convergence can actually be improved by separating out the term representing the electrons that do not interact in the path length s (Berger et al., 2007, Negreanu et al., 2005)

$$p_{\rm GS}(\Theta; s) = \exp(-\langle n\rangle)\, \frac{\delta(\cos\Theta - 1)}{\pi} + \sum_{\ell=0}^{\infty} \frac{2\ell+1}{4\pi} \left[\exp(-\langle n\rangle/\tilde{\lambda}_\ell) - \exp(-\langle n\rangle)\right] P_\ell(\cos\Theta) \ , \quad (5)$$

where δ is the Dirac δ-function. The angular integration of Eq. (4) or (5) can be evaluated analytically as presented in AppendixA.

The Goudsmit–Saunderson approach, published earlier, is an improvement over the widely-known one by Molière (1947), which makes a small-angle approximation and requires a DCS that tends to the Rutherford formula for large momentum transfers (Fernández-Varea et al., 1993). The result by Molière is however given in terms of universal functions that can be tabulated once and for all (Andreo et al., 1993), while the Goudsmit–Saunderson one requires the evaluation of the coefficients of the expansion and the Legendre polynomials for large values of n (thousands) and, lastly, of the final sum. This was impractical for routine calculations before the advent of digital computers. A very complete discussion of the similarities between the Goudsmit–Saunderson and Molière formulations in terms of a compound Poisson stochastic process, as well as of the consequences of the small-angle approximation, was published by Ning et al. (1995).

Assumption a) above essentially amounts to disregarding any effect of energy loss since the DCS is evaluated at the initial electron energy. Moreover, this assumption implies that inelastic collisions can be included only approximately by changing the DCS in Eq. (3), but the produced secondary electrons are not accounted for. Finally, assumption b) means that any correlation between the deflection angle and the average number of interactions, which is present for finite path lengths, is neglected. The latter statement suggests that the Goudsmit–Saunderson theory, when applied to electrons impinging perpendicularly on a slab of material with a finite thickness much smaller than its lateral extension, should work better in the frontal region. On the other hand, electrons scattered close to $\Theta = 90^\circ$, i.e. along the surface of the slab, see an increased path length in the medium and have a higher probability of suffering another interaction. Therefore, a conspicuous dip appears in the angular PDF around 90°. Moreover, electrons escaping the slab from the rear face due to backscattering, also have a zero probability of being scattered again in the forward direction unlike in an homogeneous environment. A comparison of the Goudsmit–Saunderson theory with the PENELOPE MC code will be presented in part II (Barros et al., 2022a), highlighting a failure of the former in the mentioned angular regions close to 90° and 180°, which we term here target finite-size effects. In a somewhat different visualisation, one can state that Eq. (4) is appropriate only for the quite paradoxical idealisation of an infinite medium where no energy loss is present and the average number of collisions remains finite.

An extension of the Goudsmit–Saunderson approach to include energy loss was introduced by Lewis (1950). Of course, it requires to know the energy dependence of the coefficients of the expansion of the DCS, see Eq. (3). Moreover, it assumes the CSDA to arrive at a one-to-one correspondence between the path length s and the energy lost by the electron. This is a reasonable approximation as long as the energy loss is a small fraction of the initial energy. The latter issue, together with the neglect of the correlation between the number of collisions and the deflection angle, implicit in the Goudsmit–Saunderson formulation, means that electrons that are fully stopped inside a finite slab, especially in a direction where the apparent thickness is increased, cannot be handled by the Lewis theory. The presence of secondary electrons continues to be ignored in the Lewis approach, as it is in the Goudsmit–Saunderson formalism. Then, inelastic collisions can be only partially accounted for by taking the DCS in Eq. (3) to be the sum of the elastic and inelastic ones.

From the practical point of view, the calculations reported here in comparison with the integral measurements, have been carried out with the programs distributed together with the ICRU Report 77 (Berger et al., 2007). We assume that the path length s is the same as the target thickness. The integrations of the MS angular distributions over the acceptance angle of the Faraday cup and the ring have been done with the Mathematica® 11.3 software by interpolating the tables generated by the ICRU Report 77 programs and then performing a numerical quadrature. Such a procedure has been tested against the exact analytical integral of the Goudsmit–Saunderson distribution as described in AppendixA. The programs of the ICRU Report 77 (Berger et al., 2007) only tabulate the regular part of $p_{\mathrm{GS}}(\Theta; s)$ on a discrete angular grid; thus, the fraction of the incident beam that eventually passes through the target without interacting, corresponding to the Dirac δ-function in Eq. (5), is not included. To reproduce the experimental conditions, where such a fraction of electrons that did not interact is collected in the Faraday cup as well, it must be added separately to the numerical quadrature.

Another ingredient that needs to be specified, and indeed a very important one, is the origin of the DCSs. These have also been taken from the ICRU Report 77 (Berger et al., 2007) for the present calculations. They are actually the most accurate publicly available complete set of elastic DCSs covering all elements with atomic numbers from $Z = 1$ to $Z = 103$, for electron energies between 50 eV and 100 MeV. They have been prepared with the ELSEPA code (Salvat et al., 2005) and are also distributed as the NIST Standard Reference Database Number 64 (Jablonski et al., 2016). The basic method for the calculation, at the energies of interest here, is a partial-wave solution of the Dirac equation in a central potential, whose static part is obtained from a nuclear point-like contribution plus a Dirac–Fock self-consistent procedure for the electronic one. Therefore, the potential describes accurately an isolated atom and not e.g. a crystalline solid, since the formation of delocalised valence and conduction bands is not accounted for. Exchange effects have also been included with a Furness and McCarthy (1973) semi-empirical potential. On the other hand, polarization effects can be disregarded for the energy range of concern. The status of the validation with comparisons to data is described in the ICRU Report 77 being overall rather good. However, note that for the energy range of interest here, only one set of experimental results for Hg (Kessler and Weichert, 1968) is considered.

As mentioned, the role of inelastic collisions can approximately be accounted for by replacing the DCS in Eq. (3) with the sum of the elastic DCS and the inelastic angular DCS. In such a simplistic procedure, the highest energy electron after the inelastic collision is interpreted as the impinging one undergoing scattering, and the DCS is referred to this particular particle in the final state, neglecting all other secondary ones (although, of course, electrons are quantum-mechanically indistinguishable). This brings in the question of how to calculate inelastic DCSs. Unfortunately, fully realistic approaches are extremely CPU-time consuming, since each shell must be considered separately in heavy numerical computations, and no generally accepted solution exists. One notable step forward is the NIST Standard Reference Database Number 164 (Llovet et al., 2014), which, however, still contains only angle-integrated cross sections and does not cover all shells of all atoms. The programs distributed with the ICRU Report 77 implement a simpler philosophy. In the plane-wave Born approximation, the inelastic DCS assumes a universal form which contains, as only unknown quantity, the generalised oscillator strength (GOS) (Fano, 1963, Fernández-Varea et al., 2005, Berger et al., 2007, Negreanu et al., 2005). It is not much of a change, unless a simple analytical form is found for the GOS. Such a way out has been proposed by Liljequist (1983), who also suggested that

the needed parameters should be determined following the prescriptions developed by Sternheimer (1952, 1953) for the calculation of the density-effect correction to the electronic stopping power. The GOS approach can be extended to provide angular DCSs (integrated over the energy lost by the impinging electron) as well (Fernández-Varea et al., 2005, Negreanu et al., 2005). We employ such a model, which we refer to as the Sternheimer–Liljequist one, as implemented in the programs distributed with the ICRU Report 77 (Berger et al., 2007) mostly to assess the magnitude of the corrections that can be expected from including inelastic collisions.

Finally, for the Lewis approach, it is necessary to incorporate electron energy loss in the CSDA. The programs distributed with the ICRU Report 77 (Berger et al., 2007) implement the tabulation of the ICRU Report 37 (Berger et al., 1984), also available as part of the NIST Standard Reference Database Number 124 (Berger et al., 2017). One additional parameter is actually included in the Sternheimer–Liljequist model and tuned to achieve consistency with the ICRU Report 37 values of the Bethe mean excitation energy (Berger et al., 2007, Negreanu et al., 2005).

4. Monte Carlo simulation

A simple MC code that simulates in a detailed way all elastic collisions in the target has been compared with the experimental data and, most importantly, used to propagate the experimental uncertainties (see Sec. 5). The code was actually developed to include the effect of more than one interaction on the angular distribution of characteristic x-rays from the L_3 subshell for studying atomic alignment by electron impact (Barros et al., 2019). Inelastic collisions are not simulated and thus no secondary-particle stack is necessary: one impinging electron history can be followed from its entrance into the target to its exit from the front or the back surfaces. Since the energy loss is not included, the impinging electron energy remains constant along the trajectory and the output of one simulation history is the sequence of interaction points inside the target and the direction versor after the interaction (the first point is always the entrance point in the target and the direction versor of incidence). The approximation of neglecting secondary electrons and energy loss will be checked against experimental data for the target thicknesses considered in the experimental study in Sec. 6. As in the case of the Goudsmit–Saunderson and Lewis analytical theories (See Sec. 3), the effect of the inelastic collisions could have been included in an approximate way by changing the DCS, but this has not been done for reasons that will be explained in Sec. 6. The algorithm is rather transparent and it has been implemented in the same Mathematica® 11.3 software chosen for the rest of the analysis work.

The handling of the geometry is greatly simplified by considering targets made of parallel slabs only (the initial incidence is not constrained to be perpendicular). The developed program has provision for two kinds of targets: the self-supporting ones, made of only one material, and those deposited on a substrate, constituted by two layers of different compositions. The elastic DCSs are the same as the ones used in the Goudsmit–Saunderson and Lewis theories to allow a meaningful comparison, namely those included with the ICRU Report 77 (Berger et al., 2007). In one case, the Bi_2O_3/C target, it is necessary to account for the presence of the two different atomic species. This has been handled in an approximate way by resorting to the Bragg additivity rule (Negreanu et al., 2005).

The developed code has been validated by comparison with the Goudsmit–Saunderson analytical approach, once the employed DCSs are the same. The general overall agreement is rather good, matching the estimated statistical uncertainties, when target finite-size effects are not important.

5. Data Analysis

To analyse the data, it is first necessary to ascertain if any drift of the beam happened from the initial focusing and then to correct the ratios $R_{\rm FC}$ and $R_{\rm R}$ for the fraction of electrons incident on the Faraday cup and the ring that are backscattered by these structures. Finally, the uncertainties from all sources have to be combined to arrive at an overall estimate, fundamental when judging discrepancies from any theory to be presented in Sec. 6.

5.1. Determination of the charge fractions

As discussed in Sec. 2.3, an important aspect of the experiment is to ensure that the beam is initially properly focused on the target and then remains stable without drifting. The first condition is checked, as already described, with the hollow frames. The ratios $R_{\rm FC}$ and $R_{\rm R}$ are not affected by fluctuations of the beam current but, on the other hand, they are sensitive to small drifts of the beam position (possibly resulting from energy variations). During the runs, the time dependence of the currents measured in the Faraday cup, the ring, and the chamber are stored. Then the time variation of $R_{\rm FC}$ and $R_{\rm R}$, see Eqs. (1), are analysed off-line to inspect for small systematic drifts. As a by-product, the procedure allows to estimate their uncertainties as well.

In a first step, the parameters of a zero-th ($p_0(t) = a_0$) and a first ($p_1(t) = a_1 + b_1\, t$) degree polynomial are fitted to the values of $R_{\rm FC}$ and $R_{\rm R}$ recorded over the time span of the run. At this stage, it is assumed that all points have the same uncertainty. Imposing the condition that the reduced chi-square of the fit with each polynomial must be equal to one, it is possible to obtain an estimate of the standard deviations σ_0 and σ_1 for the fit of the parameters of p_0 and p_1, respectively.

As a second step, it is necessary to decide if the data are better reproduced by the p_0 or p_1 model function. The choice of the most suitable degree of a polynomial to be fitted to a data set has a standard solution described in textbooks on statistics (Eadie et al., 1971). It is based on comparing σ_0 and σ_1 taking into account their uncertainties given by the standard deviation of the standard deviation (Eadie et al., 1971)

$$\sigma_{\sigma_i} \equiv \frac{\sigma_i}{\sqrt{2(N-1)}} \ , \tag{6}$$

where N is the number of points in the data set. If $r_{01} \equiv \sigma_0/\sigma_1$ is compatible with 1 within $5\,\sigma_r$ where

$$\frac{\sigma_r}{r_{01}} \equiv \sqrt{\left(\frac{\sigma_{\sigma_0}}{\sigma_0}\right)^2 + \left(\frac{\sigma_{\sigma_1}}{\sigma_1}\right)^2} \quad , \tag{7}$$

then the lower-degree polynomial p_0 has to be chosen to describe the data set, and, in turn, it is concluded that the analysed charge fraction remains constant in time. On the other hand, whenever r_{01} differs from 1 by more than $5\,\sigma_r$, the charge ratio cannot be assumed to be constant and the data set is discarded under the assumption of a drift of the beam position. An example of these two situations is offered by the Te/C target irradiated with 33.00 keV electrons: r_{01} is 1 within $\approx 1\,\sigma_r$ for both $R_{\rm FC}$ and $R_{\rm R}$, while for the same target irradiated with 12.59 keV electrons, r_{01} deviates from 1 by more than $\approx 10\,\sigma_r$ for $R_{\rm R}$ but continues compatible with 1 within $\approx 1\,\sigma_r$ for $R_{\rm FC}$. To ease the visualisation, Figure 6 compares the $R_{\rm R}$ residues for p_0 and p_1 during the irradiations at 12.59 and 33.00 keV, in the upper and lower panels, respectively. The different behaviour is very clear: in the lower panel both p_0 and p_1 give rather similar results and thus the simplest model p_0 has to be preferred; in the upper panel the constant behaviour p_0 does not fit well the data and, as a consequence, blows up the estimate of the uncertainty.

In the third and last step, for the accepted datasets, $R_{\rm FC}$ and $R_{\rm R}$ have been obtained from the parameter of p_0 fitted to the measurements, while their uncertainties are also given by the fitting procedure (estimated as 1 standard deviation).

5.2. *Corrections to the recorded charges*

As discussed in Sec. 2.3 and, in particular, as shown in Fig. 5, the Faraday cup backscatters a small fraction $f_{\rm FC}$ of the incident electrons that end up being collected by the chamber or the graphite ring (also connected to the chamber): it is $f_{\rm FC} \approx 2\%$ for 10 keV electrons dropping to $f_{\rm FC} \approx 0.7\%$ at 100 keV. The value of $f_{\rm FC}$ measured with the hollow frames in the same run is used to correct Eqs. (1) when the targets are present: $f_{\rm FC}$ is added back to $Q_{\rm FC}$ and subtracted from $Q_{\rm C}$ (hence the denominator is not changed). The uncertainty on $f_{\rm FC}$ is assumed to result solely from the measurement process with the hollow frames and is thus given by the same fitting procedure described in Sec. 5.1 for $R_{\rm FC}$ in the case when a target is present.

The fraction of the charge incident on the aluminium ring that is backscattered, $f_{\rm R}$, can not be measured with the same procedure employed for $f_{\rm FC}$. As a matter of fact, using data collected with the hollow frames, it is not possible to detect the charge incident on the ring and thus to separate the contribution of the charge backscattered by the ring to the one collected by the chamber. A dedicated measurement has been performed before those with the targets: a plate, with a dimension of 15 cm by 15 cm, made of the same aluminium that has been used to built the ring (since this material is actually an alloy with small contents of other metals), has been installed inside the chamber in front of the ring, actually closing the entrance of the Faraday cup. The beam has then been made to impinge directly on the aluminium plate without a target present: it is therefore possible to assume that all the beam

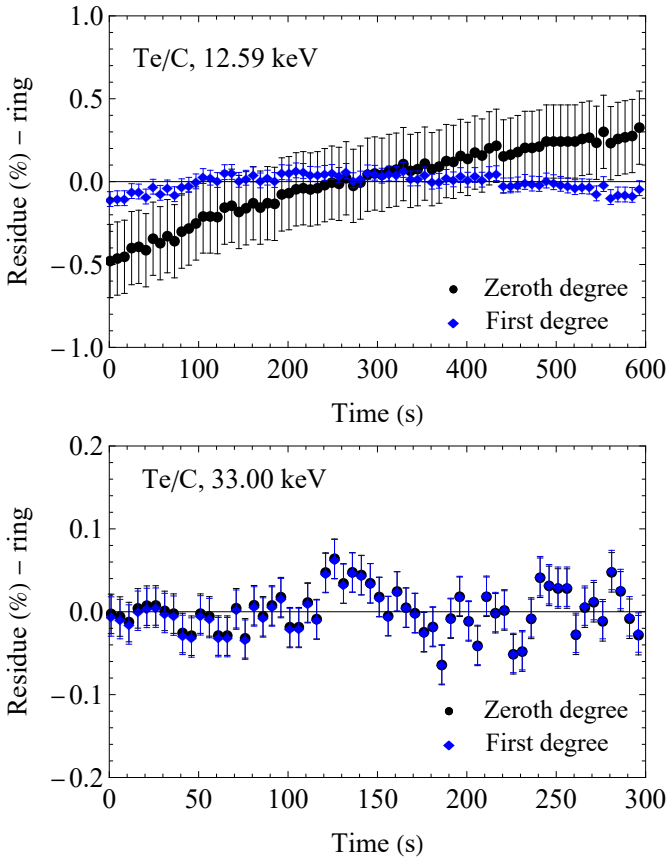

Figure 6: Residues of the fit of the parameters of a zeroth degree, p_0, and a first degree, p_1, polynomials to the recorded time dependence of $R_{\rm R}$, Eqs. (1), for the Te/C target irradiated with 12.59 keV (upper panel) and 33.00 keV (lower panel) electrons. The black dots and blue diamonds refer to p_0 and p_1, respectively. In the upper panel, the variation with time is very clear and a fit with a constant, p_0, blows up the estimated uncertainty. On the other hand, in the lower panel, the diamonds are almost always on top of the dots and can hardly be distinguished.

current hits the plate and that the charge collected by the chamber has been backscattered by the former. The results are shown in Fig. 7. Actually, this is a backscattering configuration and the values can be compared with published data for the same conditions (Bishop, 1966, Cosslett and Thomas, 1965, Drescher et al., 1970, Neubert and Rogaschewski, 1980). Simulations have also been made with the PENELOPE code (Baró et al., 1995, Sempau et al., 1997, Salvat, 2015), both by us (PENLOPE version 2018 (Salvat, 2019)) and by Sempau et al. (2003) (with an older version of PENELOPE), and an empirical parameterisation of many experiments with different target materials has been proposed by Tabata et al. (1999): they are included as well in Fig. 7. The good agreement of PENELOPE with the data confirms the reliability of the simulations, which have then been used to evaluate the effect of the angle of incidence. In fact, as it is visible from Fig. 4, the electrons from the target hit the surface of the ring with an angle from the perpendicular direction varying between $\Theta_{\rm R_i}$ and $\Theta_{\rm R_o}$. We do not have an easy way to do the measurements with the aluminium plate inclined by a well-controlled angle. Therefore, the final correction factor has been taken as the average of the simulated backscat-

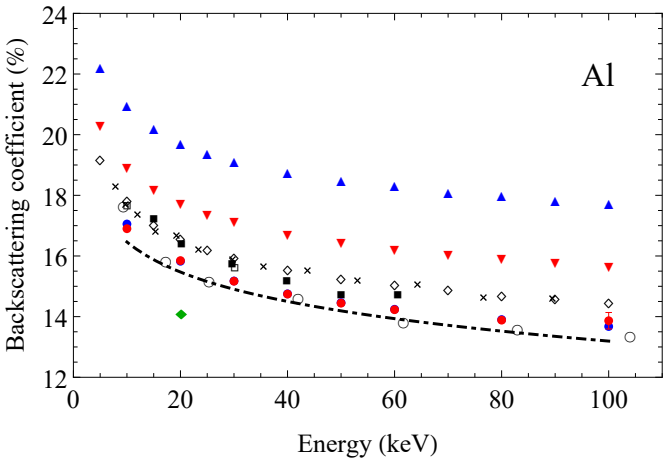

Figure 7: Fraction of the incident electrons backscattered by bulk Al: the solid dots (blue and red) have been measured with an aluminium plate placed in front of the Faraday cup perpendicularly to the beam, while the empty circles (Drescher et al., 1970), filled squares (Neubert and Rogaschewski, 1980), filled diamond (Cosslett and Thomas, 1965) and the empty square (Bishop, 1966) are published experimental results under the same conditions. PENELOPE 2018 (Salvat, 2019) simulations are represented with open diamonds, those with an older version of PENELOPE by Sempau et al. (2003) are shown with crosses, and the semi-empirical parameterisation by Tabata et al. (1999) is displayed with a dashed curve. They all refer to perpendicular incidence. Finally, PENELOPE simulations with a beam incident at $\Theta_{R_i} = 14.4°$ and $\Theta_{R_o} = 23.5°$ from the normal direction are plotted with filled downward and upward triangles, respectively.

tering coefficients considering the two extremes Θ_{R_i} and Θ_{R_o}. Again, the average of the simulated f_R in the backscattering configuration is added back to Q_R and subtracted from Q_C to correct Eqs. (1) when the targets are present. The uncertainty on f_R, which is larger than that on f_{FC}, has been estimated as the difference between the two limiting values at an incidence of Θ_{R_i} and Θ_{R_o} (considering that the angular distribution is non-uniform and changes with target and energy from rather open to narrowly forward concentrated, see Sec. 6).

To summarise, the calculated values have to be compared with the corrected experimental ratios

$$\begin{aligned} F_{FC} &\equiv \frac{Q_{FC}}{Q_{FC}+Q_R+Q_C}\,(1+f_{FC}) \\ &= R_{FC}\,(1+f_{FC}) \ , \\ F_R &\equiv \frac{Q_R}{Q_{FC}+Q_R+Q_C}\,(1+f_R) \\ &= R_R\,(1+f_R) \ , \end{aligned} \tag{8}$$

which should actually be substituted for R_{FC} and R_R in Eqs. (2).

5.3. *Combined uncertainty*

Besides the uncertainty associated with the charge measurement, estimated as described in Sec. 5.1, and with the corrections necessary to account for the fractions that are backscattered, estimated as described in Sec. 5.2, there are other sources that affect F_{FC} and F_R: namely the uncertainty on the areal density of the target and C backing, see Sec. 2.1, and those on the solid angle covered by the Faraday cup and the aluminium ring, see Sec. 2.2. All the contributions have been combined using the standard propagation methodology (Eadie et al., 1971) as

$$\boldsymbol{V}_f = \boldsymbol{V}_{exp} + \boldsymbol{D}\,\boldsymbol{V}_{par}\,\boldsymbol{D}^T, \tag{9}$$

where $\boldsymbol{V}_{exp}$ is a diagonal matrix with the sum of the variances estimated in Secs. 5.1 and 5.2, $\boldsymbol{V}_{par}$ is a diagonal matrix with the variances of the areal densities, see Sec. 2.1, and the limiting angles of the Faraday cup and the ring, see Sec. 2.2, and $\boldsymbol{D}$ is a rectangular matrix whose elements are the derivatives of $F_i = (F_{FC}, F_R)$ with respect to the mentioned angles or areal density (represented by the vector $\boldsymbol{y}$)

$$D_{ij} \equiv \frac{\partial F_i(\boldsymbol{y})}{\partial y_j} \ , \tag{10}$$

evaluated at the experimental values. The partial derivatives in Eq. (10) have been calculated numerically, using for F_i the curve as a function of y_j obtained by running several times the MC code described in Sec. 4 with different values of y_j.

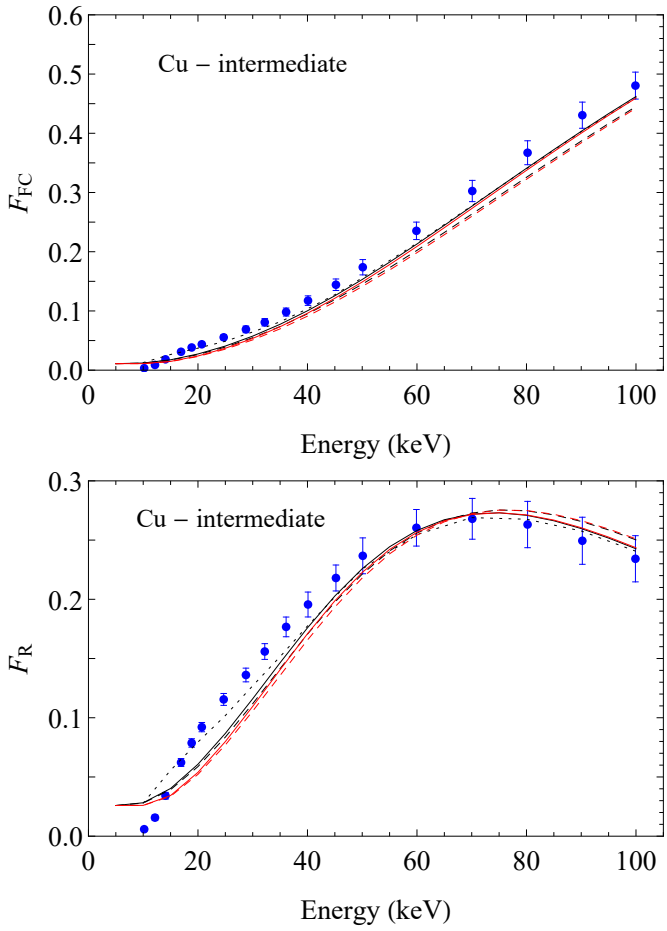

Figure 8: Ratios F_{FC} and F_R, see Eqs. (8), for the intermediate Cu target. The dots with uncertainty bars (representing 1 standard deviation) are the data. The curves have been calculated with the MC code (black dotted), the Goudsmit–Saunderson approach with elastic DCSs (black continuous), the Goudsmit–Saunderson approach with elastic plus inelastic DCSs (black dashed), the Lewis approach with elastic DCSs (red continuous), and the Lewis approach with elastic plus inelastic DCSs (red dashed).

6. Results and discussion

The experimental values of F_{FC} and F_{R} for the thin (C, Al/C, Cu/C, Te/C, Au/C, and Bi_2O_3/C) and intermediate (Al, Cu, and Au) targets irradiated with electron energies between 10 and 100 keV are given in the supplemental material. All the corrections described in Sec. 5.2 have been included. The combined standard deviations, according to the procedure described in Sec. 5.3, are also reported.

The case of the intermediate Cu target is displayed in Fig. 8. The general trend of F_{FC} is common to all other cases not shown: with increasing beam energy it grows towards one, as is expected when the MS distribution $p_{\mathrm{MS}}(\Theta)$ is more and more narrowly concentrated at small Θ. The maximum of F_{R} has the same origin. Initially, at low energies, $p_{\mathrm{MS}}(\Theta)$ is rather open and the fraction of electrons collected by the ring is small. Then, with increasing energy, $p_{\mathrm{MS}}(\Theta)$ starts to peak in the forward direction eventually going through a condition where it is focused in the Θ range $(\Theta_{\mathrm{R_i}}, \Theta_{\mathrm{R_o}})$ covered by the ring, producing the maximum of F_{R}. Finally, when the beam energy grows even further, the forward focusing of $p_{\mathrm{MS}}(\Theta)$ continues and most of the beam is collected by the Faraday cup resulting in the decrease of F_{R}. Actually, for the thin targets, only the decreasing part of F_{R} has been scanned by the present experiment, with indications of a maximum located at the second lowest measured energy for the Cu/C and Te/C cases. The maximum appears instead well inside the covered range at $\approx$ 30, $\approx$ 70, and $\approx$ 40 keV for the intermediate Al, Cu, and Au targets, respectively (see also Fig. 6 by Martins et al. (2022)).

As it is clearly visible in Fig. 8, the calculations are rather close to the experiment, therefore to better display systematic discrepancies, we have chosen to plot only the deviations from the common smooth behaviour of the data. No simple general expression for the dependence of F_{FC} and F_{R} on energy is available, therefore we have decided to use a polynomial, whose parameters are fitted to the measurements. The degree of the polynomial is determined according to two criteria.

The first criterion is based on the estimation of the variance of the data, σ^2_{p}. For the polynomial p_n of degree n, whose coefficients have been fitted to the data themselves, the variance is defined in the usual way as

$$\sigma^2_{\mathrm{p}}(n) \equiv \frac{1}{m-n-1} \sum_{i=1}^{m} \frac{\left(F_{\mathrm{exp}_i} - p_n(e_i)\right)^2}{\sigma^2_{\mathrm{exp}_i}} \quad , \qquad (11)$$

where m is the number of values of the ratio F_{exp_i} with standard deviation σ_{exp_i} measured at the beam energies e_i. Then, using Eq. (11), the quantity

$$(m-n-1)\,\frac{\sigma^2_{\mathrm{p}}(n-1) - \sigma^2_{\mathrm{p}}(n)}{\sigma^2_{\mathrm{p}}(n)} \qquad (12)$$

has a PDF of the Fisher type (Eadie et al., 1971) $F(1, m-n-1)$. It is then possible to estimate the significance of the term of order n in the polynomial. In all cases, the degree of the polynomial has been chosen to be less or equal to that indicated by the statistical test described with a significance of 95%.

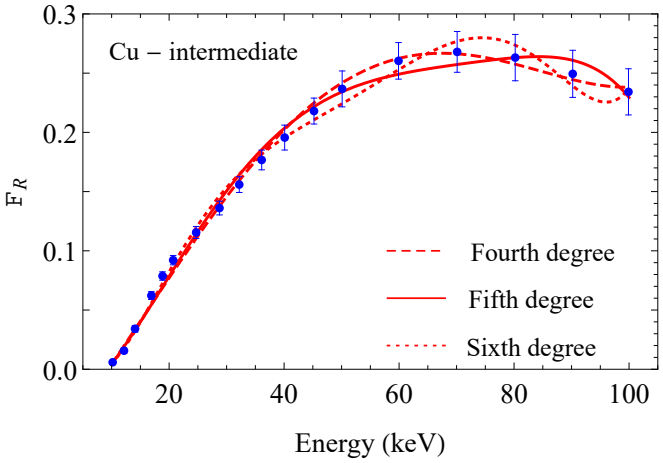

Figure 9: Values of F_{R} for the Cu target as a function of the beam energy. The points with uncertainty bars (representing 1 standard deviation) are the data. The continuous curves are the results of polynomials (see legend for the degree), whose parameters have been fitted to the data.

In the present work, however, the number of fitted points m is relatively small when compared to the degree of the polynomial, n, necessary to explain their behaviour according to the criterion just described. A possible risk of over-fitting, i.e. of trying to reproduce random fluctuations of the data, is hence present. A generally-accepted guideline is that the test described with the Fisher PDF is applicable when m is 4 to 5 times larger than n (Draper and Smith, 1998). Therefore, another criterion has been added requiring that the second derivative of the polynomial can change sign only once in the whole energy interval considered.

In $\approx$ 40% of the datasets (i.e. targets), the test with the Fisher PDF is enough to guarantee a smooth second derivative; in the others, n has been successively lowered by one with respect to the value suggested by the statistical test until the smoothness of the second derivative is ensured. Figure 9 illustrates one of the worst cases: that of F_{R} for the Cu target. The effect of over-fitting appears very clearly when looking at the case $n = 6$: the oscillations in the polynomial are likely caused by the reproduction of random fluctuations of the points. In the case of Fig. 9, both criteria require to exclude $n = 6$. However, the choice between $n = 4$ and $n = 5$ is harder to make by eye: only the statistical test based on Eq. (12) allows to select $n = 5$. In general, for all datasets, the final n is between 4 and 7, with the worst case being F_{R} for the Cu/C target where $n = 9$. For the sake of completeness, the coefficients of the polynomial obtained from the fitting procedure are given in the supplemental material.

The polynomial, whose coefficients have been fitted to the data, is then used to subtract the common smooth behaviour from the data themselves, the simulations carried out with the MC described in Sec. 4, and, when present, the results obtained with the Goudsmit–Saunderson and Lewis analytical approaches discussed in Sec. 3. Note that, in this way, any bias towards a particular theory is prevented and the horizontal zero corresponds to the best possible estimate of the experimentally

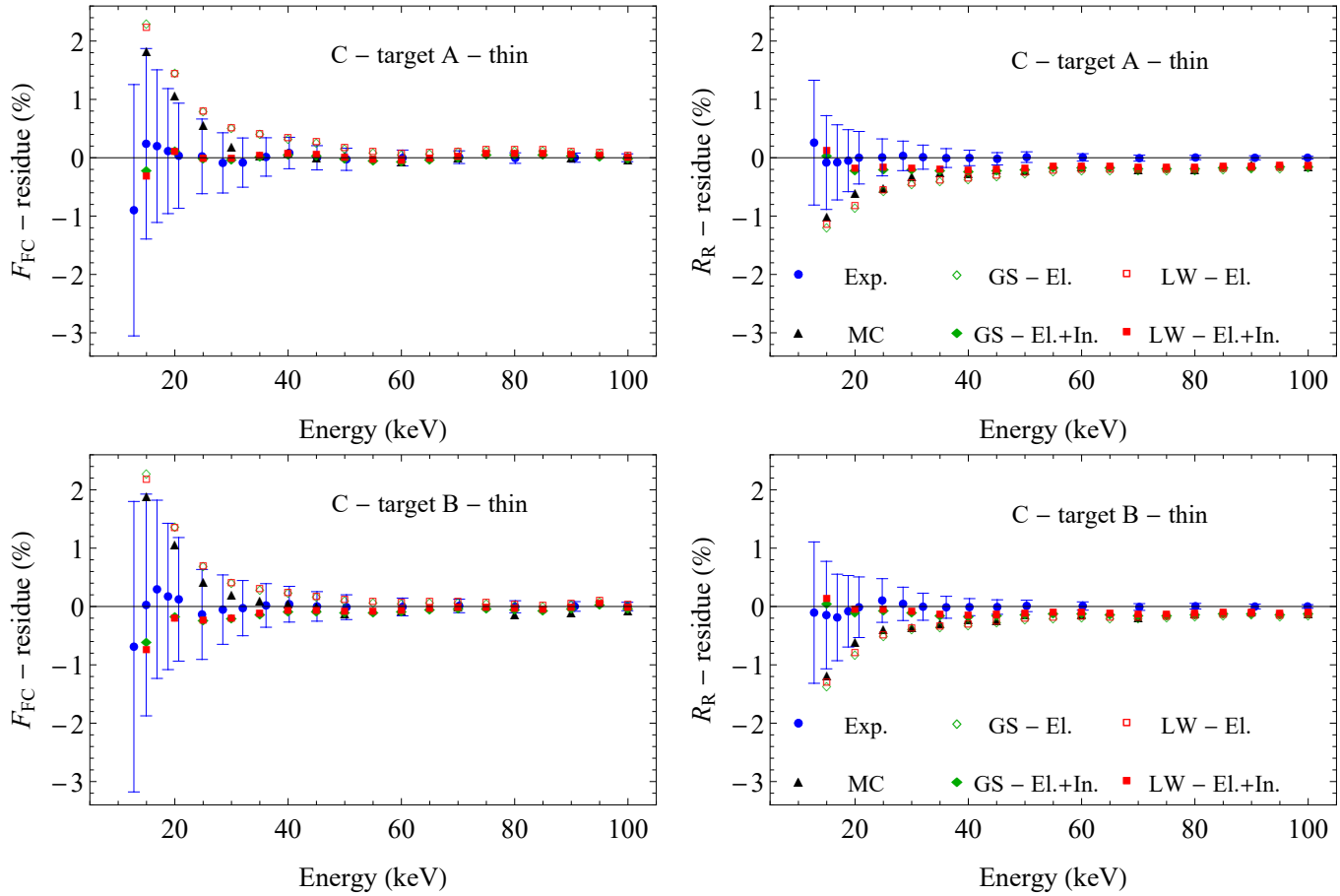

Figure 10: Deviations of F_{FC} and F_R, Eqs. (8), from the polynomial fit described in the text as a function of the beam energy for the thin C targets. The symbols with uncertainty bars (representing 1 standard deviation) are the data, while all others are simulations or calculations (see the legend).

observed trend. To save space, only these difference plots are depicted in Figs. 10, 11, 12, and 13, but, as mentioned, to avoid hindering any independent comparison with the present measurements, the values before applying the subtraction with the polynomial are given in the supplemental material.

All targets considered in the present work are thin enough to allow the direct (event-by-event) simulation of all individual elastic collisions and the results are included in Figs. 10, 11, and 12, for the thin targets, and in Fig. 13, for the intermediate ones. The values obtained from such time-consuming detailed MC are also provided in the supplemental material. A comparison with the general-purpose PENELOPE MC code, which takes into account energy loss, is presented for thin, intermediate, and thick targets in part II (Barros et al., 2022a). For the cases composed of a single element, namely the thin carbon targets, see Fig. 10, and the intermediate targets, see Fig. 13, the Goudsmit–Saunderson and Lewis theories are applicable and are considered as well. We assume that the path length s is the same as the target thickness. The cases where elastic only and elastic plus inelastic DCSs (employing the Sternheimer–Liljequist model) have been considered, appear separately in Figs. 10 and 13 (open versus closed symbols, respectively). The overall agreement between calculations and data continues to be rather good, even in this expanded view, considering the uncertainty bars of the latter. Some more detailed comments are in order.

For the thin C targets, see Fig. 10, the MC simulations agree very well with both the Goudsmit–Saunderson and Lewis analytical theories when elastic DCSs are selected. In fact, no energy loss or finite-size effects are expected for such small areal densities of atoms with low Z. The importance of the inelastic DCS relative to the elastic one is the largest amongst all the elements considered in the present study, since Z is the lowest. Indeed, the Goudsmit–Saunderson and Lewis results, including the inelastic DCSs, are closer to the data than those with elastic DCSs only.

For the other thin targets (Al/C, Cu/C, Te/C, Au/C, and Bi_2O_3/C), which are not homogeneous, see Figs. 11 and 12, only the MC simulations employing elastic DCSs have been performed. The inelastic DCSs have not been considered since no consistent picture could be obtained with their inclusion for the simpler case of homogeneous intermediate targets (see below). The simulations including the amount of oxygen reported in Table 1 are also shown separately in Fig. 13 for the Al/C and Cu/C targets (compare the upward and downward triangles, without and with oxygen, respectively). The worst case is that of Al, where the oxygen fraction is largest and the difference in atomic number the smallest: in general, the impact of the con-

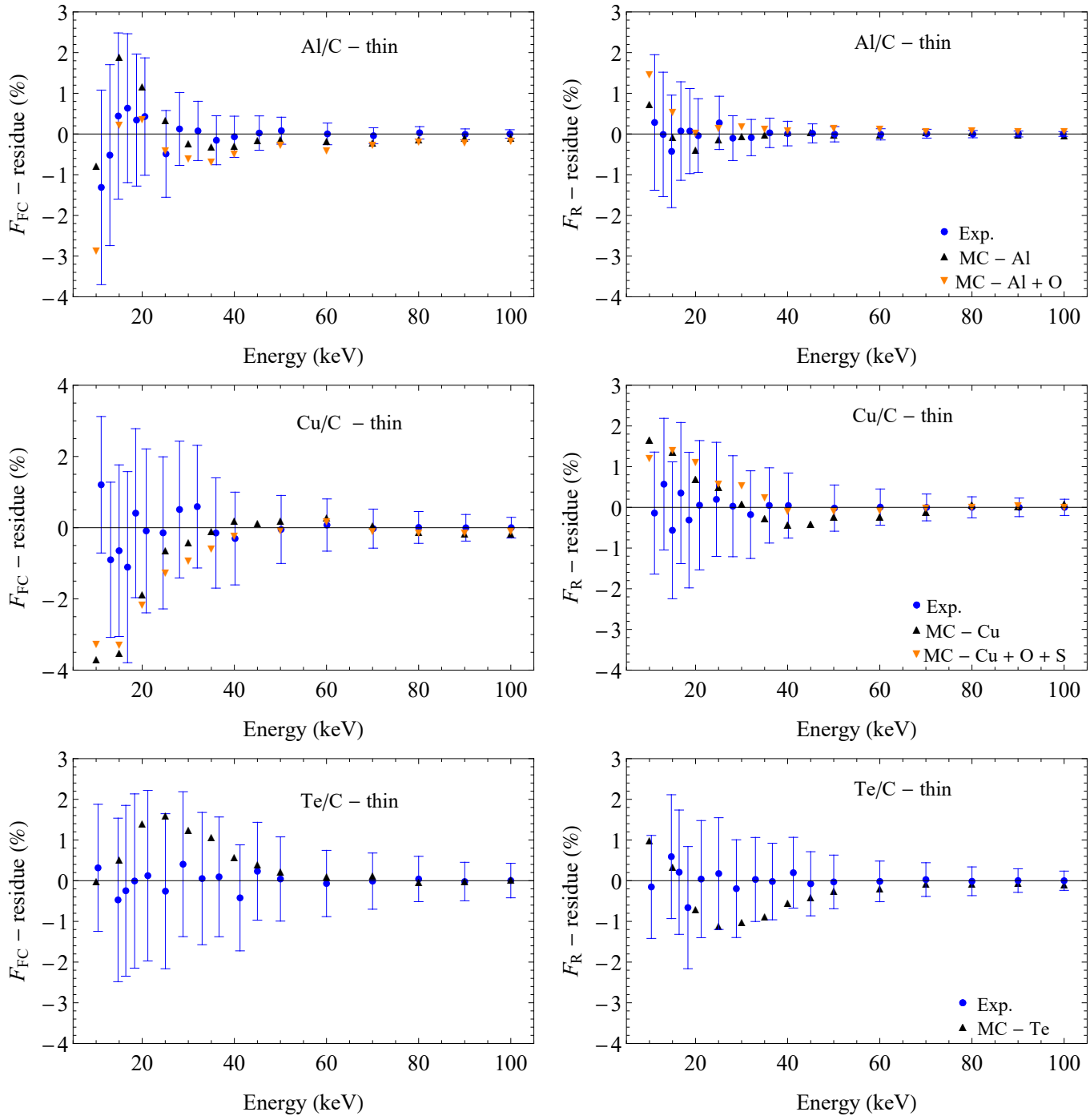

Figure 11: Deviations of F_{FC} and F_R, see Eqs. (8), from the polynomial fit described in the text as a function of the beam energy for the thin Al/C, Cu/C, and Te/C targets. The symbols with uncertainty bars (representing 1 standard deviation) are the data, while all others are simulations (see the legend). The effects of the contaminants, see Table 1, are shown with a separate simulation only for the worst cases of Al/C and Cu/C.

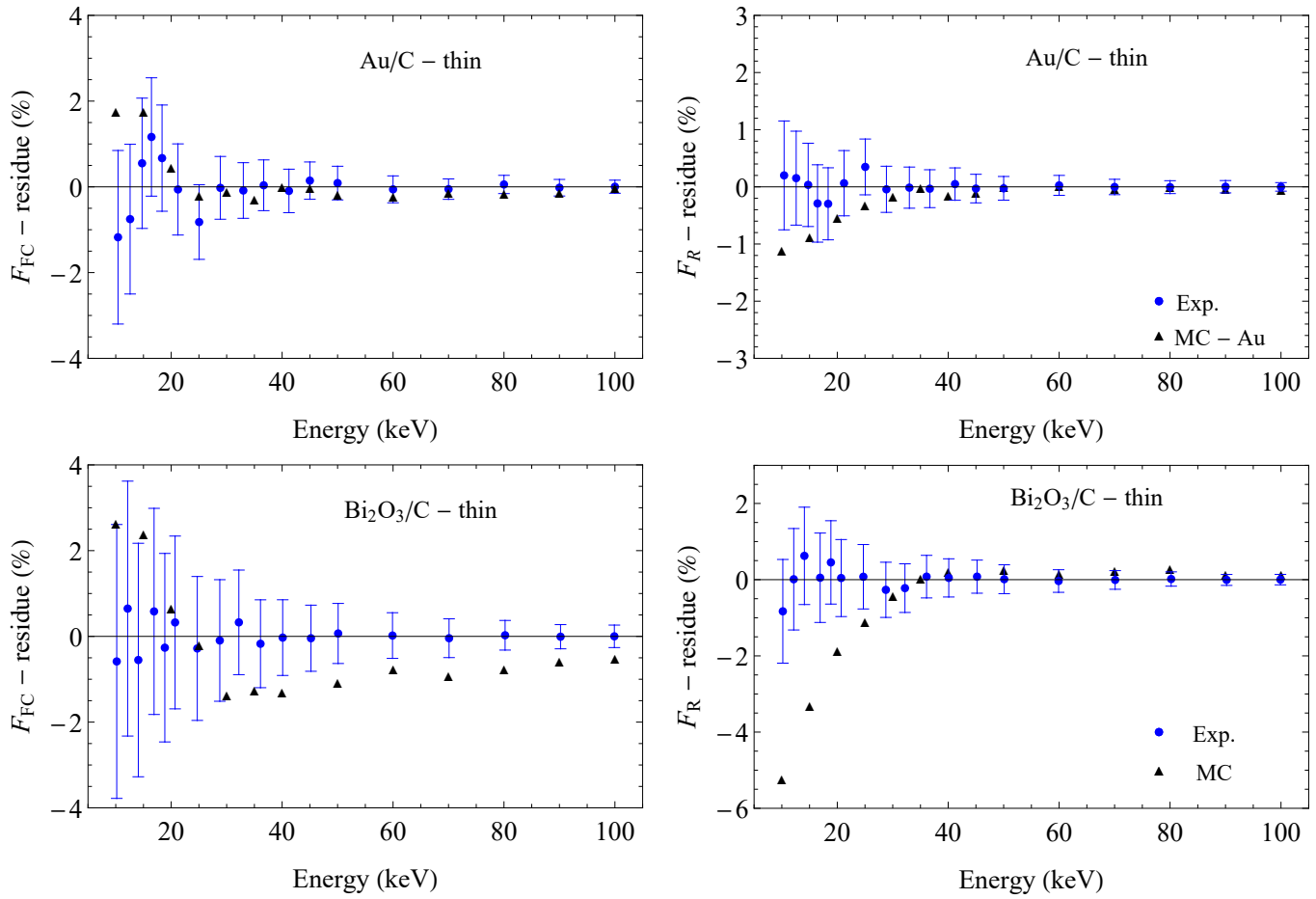

Figure 12: Deviations of F_{FC} and F_R, see Eqs. (8), from the polynomial fit described in the text as a function of the beam energy for the thin Au/C and Bi_2O_3/C targets. The symbols with uncertainty bars (representing 1 standard deviation) are the data, while all others are simulations (see the legend).

taminant grows towards the lowest energies, but the deviations remain, in all cases, within the combined uncertainties of the data. For Cu, the difference in atomic number is already big enough to render the influence of the contaminants, in terms of DCSs, small. Even more so is the case for the other elements. For all the thin targets, the overall agreement between simulations and experiment is again very good, considering the magnitude of the uncertainty bars. The only possible exception being Bi_2O_3/C, see Fig. 12: in particular, for F_{FC} at higher electron energies and F_R in the complementary lower range. The element Bi has the highest Z amongst all those covered in the present investigation and the relative importance of the inelastic DCS is expected to be the lowest. On the other hand, inelastic collisions are more important in O. In search of possible explanations, we have also checked that 10 keV electrons (the worst case) loose 2.6% and 0.5% of their energy in the C and Bi_2O_3 layers, respectively, according to the tabulations given in the ICRU Report 37 (Berger et al., 1984). Already at 20 keV, these values are down to 0.8% and 0.2%, respectively. Thus, the approximation in the MC of assigning the initial energy to all the electrons along the whole trajectory is fully justified (note that a similar argument applies to all thin targets). However, one also has to question the use of the Bragg additivity rule to describe the interactions with Bi_2O_3 in the MC. Finally, genuine molecular effects on the DCSs (going beyond the isolated-atom calculations of the ICRU Report 77, see Sec. 3) may also play a role.

Lastly, the intermediate targets (Al, Cu, and Au) are displayed in Fig. 13. For these homogeneous targets, the Goudsmit–Saunderson and Lewis theories are applicable and can be compared to the MC, when only elastic DCSs are chosen: the agreement thus validating both. Quite surprisingly, the inclusion of inelastic collisions takes the calculations away from the experiment. The discrepancy has a higher significance for F_{FC}, in particular at the lower electron energies: it remains clearly present even for Au, where the relative importance of the inelastic DCS is the lowest amongst the three elements of Fig. 13. The problem appears for F_R as well, being clearly visible for Cu because the size of the uncertainty bars is smaller. As mentioned in Sec. 2.2, a movable two-ring structure has been employed in part II to make unidirectional measurements of electron flow inside the chamber. A target-generated background has been uncovered: it is caused by electrons backscattered from the target reaching the Faraday cup and the fixed aluminium ring after one more backscattering by the walls of the chamber. Its effect on the thick target data is clearly visible,

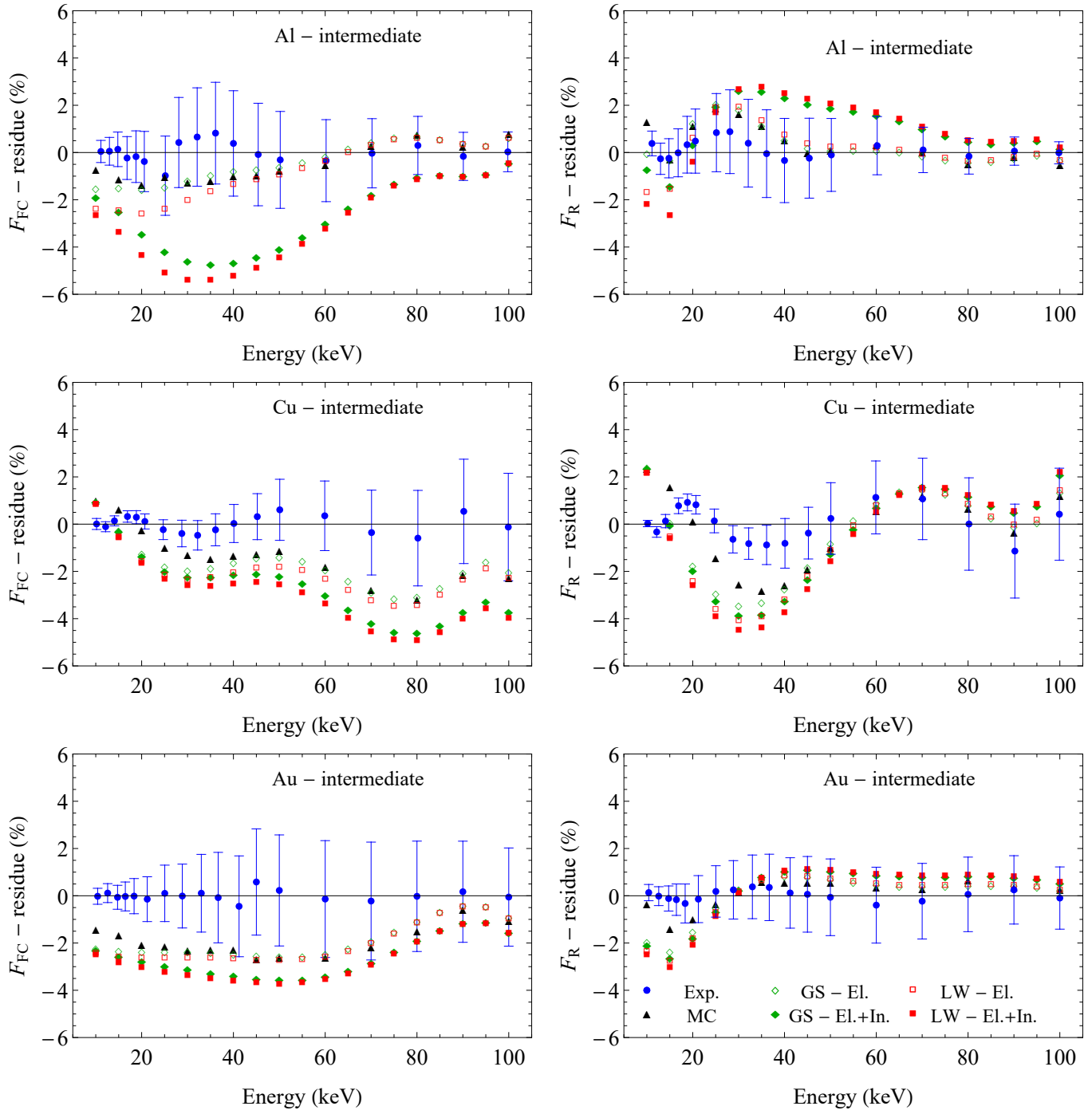

Figure 13: Deviations of F_{FC} and F_R, see Eqs. (8), from the polynomial fit described in the text as a function of the beam energy for the intermediate Al, Cu, and Au targets. The symbols with uncertainty bars (representing 1 standard deviation) are the data, while all others are simulations or calculations (see the legend).

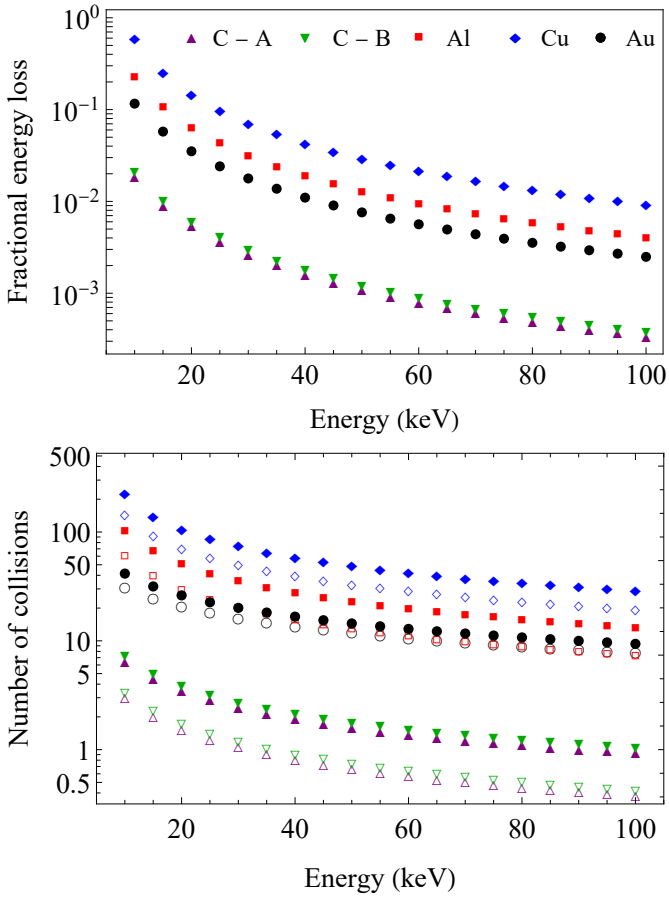

Figure 14: Fractional energy loss (upper panel) and average number of collisions $\langle n \rangle$ (lower panel) of the electrons impinging on the homogeneous targets. The values of $\langle n \rangle$ considering elastic only and elastic plus inelastic collisions are shown with open and closed symbols, respectively. No difference is present for the energy loss within the approximations employed. The results have been calculated with the program implementing the Lewis approach distributed together with the ICRU Report 77 (Berger et al., 2007).

since it diverts F_{FC} and F_{R} from zero at low energies, where all electrons should be stopped. For intermediate targets, the situation is harder to single out, but conservative estimates, based on the measurements with the two-ring system, are presented in part II and indicate that such a correction is essentially of the order of the uncertainty bars for the worst case (highest atomic number) of Au.

To better analyse the situation, the fractional energy loss and the average number of collisions $\langle n \rangle$ are reported in the upper and lower panels of Fig. 14, respectively, for all the homogeneous targets. All these values have been calculated with the program for the Lewis theory distributed with the ICRU Report 77 (Berger et al., 2007). As an example, the fractional energy losses are 23% and 60% for the Al and Cu targets and electrons energies of 10 keV, respectively. These values are not small and indeed, as mentioned, the calculations do not agree with data in the lowest energy region of Fig. 13 (for R_{FC} and Cu, the discrepancy actually extends to all energies). In the present setup, the ladder is connected to the chamber, therefore all electrons stopped in the target contribute to Q_{C} in Eqs. (8), giving one more reason, beyond the widening of $p_{\mathrm{MS}}(\Theta)$, for the decrease of R_{FC} and R_{R} at low energies in Fig. 8. Still, there is no particular evidence in Fig. 13 that the Lewis theory reproduces the measurements better than the Goudsmit–Saunderson one. The MC is closer to the experiment (see also the dotted curve in the lower panel of Fig. 8), however it is important to remember that the code does not account for the non-negligible energy loss.

The inclusion of inelastic collisions largely increases their average number (compare the full and open symbols in the lower panel of Fig. 14): $\langle n \rangle$ grows from 59 to 143 and from 100 to 222 for the Al and Cu targets at 10 keV, respectively. Even at 100 keV, the variation is from 7.2 to 13 and from 19 to 29 for Al and Cu, respectively. So much MS is possibly responsible for a too open angular distribution thus decreasing F_{FC} below the data (see the dashed curves in the higher energy region of the upper panel of Fig. 8 or compare the full and open symbols in Fig. 13). Another possibility, if the predicted increase in $\langle n \rangle$ is realistic, is that the inelastic DCSs are even more focused at small frontal angles than anticipated by the Sternheimer–Liljequist model. The reader may get the impression, by looking closer at Fig. 8, that the mentioned problem gets less severe at low energies. However, it is possibly an artefact of two limitations of the analytical approaches with opposite trends, as hinted by the disappearance of the discrepancy for the Cu target where the energy loss is largest. The almost complete absence of backscattering in the analytical approaches (see the comparison with the PENELOPE MC code in part II), which is more important at low energies, reduces the predicted fraction of charge deposited in the chamber compensating a too open forward angular distribution.

It is appropriate to highlight once more that, with the present setup, no information about the energy spectrum of the collected electrons is available: therefore, it is not possible to separate those that have been scattered elastically as well as to guarantee that the secondary ones produced in the target or in the collecting structures do not alter the final data. This state of affairs will be fully remedied only with the future differential measurements, where a low-cost PIN diode (Malafronte et al., 2021, Mangiarotti et al., 2021b) will be employed to scan the angular distribution while acquiring the energy spectra. The clarification of the role of inelastic collisions in MS has to wait until such new study is undertaken.

7. Conclusions

Integrated measurements of MS angular distributions have been performed using a Faraday cup supplemented by a ring installed around its entrance. Efforts have been devoted to optimise the setup and control systematic errors. In particular, beam focusing and drift during the measurements have been closely monitored. Electron backscattering from the collecting structures has been determined by a combination of experimental and simulation approaches and corrected for. The areal densities of the targets have been determined by a series of methods aiming at accuracy and target survival rate.

The data for the thin targets, with mass thicknesses from ≈ 5 to 20 μg/cm^2 (deposited on C backings), and for the intermediate ones, with mass thicknesses from ≈ 100 to 300 μg/cm^2, are in good agreement with MC simulations of each individual elastic collision and the Goudsmit–Saunderson and Lewis analytical theories (the latter are applicable only to the homogeneous targets). For the intermediate targets, it has not been possible to find clear evidence of any improvement brought about by the use of the Lewis formulation, accounting for energy loss, or the inclusion of the angular deflections caused by inelastic collisions into the DCSs. This may be due to the present limitation of the setup, which cannot discriminate the energy information of the collected electrons. A new setup is under preparation to better investigate the issue.

The results for thicker targets, from ≈ 1.5 to 5 mg/cm^2, will be presented and compared to MC simulations in part II (Barros et al., 2022a).

Acknowledgements

We are in debt with M.Sc. W. G. P. Engel, Dr. A. C. Tromba, and Prof. Dr. A. D. Santos for preparing the targets. This research used resources of the Laboratory of Materials Analysis with Ion Beams of the University of São Paulo (LAMFI-USP). The authors acknowledge the laboratory staff for assistance during the experiments. This work has been supported by FAPESP (Fundação de Amparo à Pesquisa do Estado de São Paulo) Grants No. 2015/14530-7 and 2016/13116-5. S. F. B. acknowledges support by FAPESP Grant No. 2013/24803-5, A. R. P. by FAPESP Grant No. 2017/12661-2, J. M. F.-V. by the Spanish Ministerio de Ciencia, Innovación y Universidades, Grant No. PGC2018-096788-B-I00, and A. M. by CNPq (Conselho Nacional de Desenvolvimento Científico e Tecnológico) Grants Nos. 306331/2016-0 and 311915/2020-5.

AppendixA. Analytical integration of the Goudsmit–Saunderson angular distribution

The Goudsmit–Saunderson expression can be integrated over a finite polar angle interval in analytical form. The method has been inspired from a similar work by Ito and Tabata (1970) for the Molière case. The cumulative distribution function of the Goudsmit–Saunderson PDF is

$$\begin{aligned}\mathcal{P}_{\mathrm{GS}}(\Theta; s) &\equiv \int_0^{\Theta} p_{\mathrm{GS}}(\Theta'; s)\, 2\pi \sin\Theta'\, \mathrm{d}\Theta' \\ &= \int_{\cos\Theta}^{+1} p_{\mathrm{GS}}(\cos\Theta'; s)\, 2\pi\, \mathrm{d}(\cos\Theta') \quad .\end{aligned} \tag{A.1}$$

Substituting Eq. (4) gives

$$\begin{aligned}\mathcal{P}_{\mathrm{GS}}(\Theta; s) = \frac{1}{2} \sum_{\ell=0}^{\infty} (2\ell+1) \exp(-\langle n\rangle/\tilde{\lambda}_\ell) \\ \int_{\cos\Theta}^{+1} P_\ell(\cos\Theta')\, \mathrm{d}(\cos\Theta') \quad .\end{aligned} \tag{A.2}$$

The integral can be evaluated analytically with the help of the relations

$$\int P_n(x)\, \mathrm{d}x = \frac{P_{n+1}(x) - P_{n-1}(x)}{2n+1} + \text{constant} \tag{A.3}$$

and

$$P_{-n}(x) = P_{n-1}(x) \qquad n \geqslant 1 \quad . \tag{A.4}$$

In particular, $P_{-1}(x) = P_0(x) = 1$. Furthermore,

$$P_n(1) = 1 \qquad \forall n \quad \text{(positive or negative)} \tag{A.5}$$

whereas

$$P_n(-1) = (-1)^n \qquad n \geqslant 0 \tag{A.6}$$

and

$$P_{-n}(-1) = (-1)^{n-1} \qquad n \geqslant 1 \quad . \tag{A.7}$$

The final expression for the cumulative distribution function is

$$\mathcal{P}_{\mathrm{GS}}(\Theta; s) = \frac{1}{2} \sum_{\ell=0}^{\infty} \exp(-\langle n\rangle/\tilde{\lambda}_\ell) \left[P_{\ell-1}(\cos\Theta) - P_{\ell+1}(\cos\Theta)\right] \quad . \tag{A.8}$$

Generalisation of Eq. (A.8) to the computationally improved Eq. (5) is straightforward.

As a cross-check of Eq. (A.8), the case $\Theta = \pi$ can be explicitly evaluated

$$\begin{aligned}\mathcal{P}_{\mathrm{GS}}(\pi; s) &= \frac{1}{2} \sum_{\ell=0}^{\infty} \exp(-\langle n\rangle/\tilde{\lambda}_\ell) \left[P_{\ell-1}(-1) - P_{\ell+1}(-1)\right] \\ &= \frac{1}{2}\, \exp(-\langle n\rangle/\tilde{\lambda}_0) \left[P_{-1}(-1) - P_1(-1)\right] \\ &\quad + \frac{1}{2} \sum_{\ell=1}^{\infty} \exp(-\langle n\rangle/\tilde{\lambda}_\ell) \left[P_{\ell-1}(-1) - P_{\ell+1}(-1)\right] \\ &= \exp(-\langle n\rangle/\tilde{\lambda}_0) = 1\end{aligned} \tag{A.9}$$

because $\tilde{\lambda}_0^{-1} = 0$, see Eq. (3).

In the present work, the PDF $p_{\mathrm{GS}}(\Theta; s)$ is tabulated for an angular grid with 606 points between $\Theta = 0$ and $\Theta = \pi$ by running the programs distributed together with the ICRU Report 77 (Berger et al., 2007). The adopted method to calculate the integral of p_{GS} takes advantage of the Mathematica built-in function Interpolation, to perform an interpolation of the third order (the default option) to the 606 values of p_{GS}, and then

Table A.1: Relative difference of the integral of p_{GS}, performed numerically with Mathematica, against the direct use of Eq. (A.8). The cases considered are 100 keV electrons impinging on the intermediate Cu and Au targets. No inelastic collisions are included in the evaluation of p_{GS}.

Target	Faraday cup	Ring
Cu	$1.5 \cdot 10^{-7}$	$-1.3 \cdot 10^{-7}$
Au	$-4.7 \cdot 10^{-8}$	$1.0 \cdot 10^{-7}$

of the function NIntegrate, to integrate numerically the interpolating function between the required solid angle limits. The procedure has been checked against Eq. (A.8), since the ICRU Report 77 programs also output the values of $\tilde{\lambda}_\ell$ according to Eq. (3). The relative differences of the numerical procedure against the exact Eq. (A.8) are reported in Table A.1 considering 100 keV electrons impinging on the Cu and Au intermediate targets. Both methods have accuracies quite adequate for the present purpose.

References

Andreo, P., Medin, J., Bielajew, A. F., 1993. Constraints of the multiple-scattering theory of Molière in Monte Carlo simulations of the transport of charged particles. Med. Phys. 20, 1315.

Baró, J., Sempau, J., Fernández-Varea, J. M., Salvat, F., 1995. PENELOPE: An algorithm for Monte Carlo simulation of the penetration and energy loss of electrons and positrons in matter. Nucl. Instrum. Methods Phys. Res. B 100, 31.

Barros, S. F., Petri, A. R., Malafronte, A. A., Fernández-Varea, J. M., Maidana, N. L., Martins, M. N., Vanin, V. R., Mangiarotti, A., 2022a. Integral measurements of plural and multiple scattering of electrons with energies between 10 and 100 keV for $13 \leq Z \leq 79$: II. Thick targets. Radiat. Phys. Chem. to be published.

Barros, S. F., Vanin, V. R., Maidana, N. L., Malafronte, A. A., Fernández-Varea, J. M., Pindzola, M. S., 2022b. Experimental and theoretical L-subshell ionization cross sections for $_{83}$Bi by electron impact from the L_3 threshold to 100 keV. Phys. Rev. A 105, 012818.

Barros, S. F., Vanin, V. R., Maidana, N. L., Martins, M. N., García-Alvarez, J. A., Santos, O. C. B., Rodrigues, C. L., Koskinas, M. F., Fernández-Varea, J. M., 2018. Ionization cross sections of the Au L subshells by electron impact from the L_3 threshold to 100 keV. J. Phys. B: At. Mol. Opt. Phys. 51, 025201.

Barros, S. F., Vanin, V. R., Mangiarotti, A., Maidana, N. L., Fernández-Varea, J. M., 2019. Atomic alignment of $_{73}$Ta, $_{74}$W, and $_{79}$Au after L_3 subshell ionization by 10–100-keV electron impact. Phys. Rev. A 100, 062705.

Berger, M. J., 1963. Monte Carlo calculation of the penetration and diffusion of fast charged particles. In: Alder, B., Fernbach, S., Rotenberg, M. (Eds.), Methods in Computational Physics. Academic Press, New York and London, p. 135.

Berger, M. J., Coursey, J. S., Zucker, M. A., Chang, J., 2017. Stopping-Power & Range Tables for Electrons, Protons, and Helium Ions, NIST Standard Reference Database Number 124, National Institute of Standards and Technology, Gaithersburg MD, 20899.
URL https://dx.doi.org/10.18434/T4NC7P

Berger, M. J., Inokuti, M., Andersen, H. H., Bichsel, H., Dennis, J. A., Powers, D., Seltzer, S. M., Turner, J. E., 1984. Report 37: Stopping Powers for Electrons and Positrons. Journal of the International Commission on Radiation Units and Measurements os19 Issue 8.

Berger, M. J., Inokuti, M., Andersen, H. H., Bichsel, H., Powers, D., Seltzer, S. M., Thwaites, D., Watt, D. E., 1993. Report 49: Stopping Powers and Ranges for Protons and Alpha Particles. Journal of the International Commission on Radiation Units and Measurements os25 Issue 2.

Berger, M. J., Jablonski, A., Bronić, I. K., Mitroy, J., Powell, C. J., Salvat, F., Sanche, L., 2007. Report 77: Elastic Scattering of Electrons and Positrons. Journal of the International Commission on Radiation Units and Measurements 7 Issue 2.

Berger, M. J., Wang, R., 1988. Multiple scattering angular deflections and energy-loss straggling. In: Jenkins, T. M., Nelson, W. R., Rindi, A. (Eds.), Monte Carlo Transport of Electrons and Photons. Plenum, New York, p. 21.

Bishop, H. E., 1966. Some electron backscattering measurements for solid targets. In: Deschamps, P., Philibert, J., Castaing, R. (Eds.), Optique des rayons X et microanalyse: IVe Congrès international sur l'optique des rayons X et la microanalyse, Orsay, 7-10 Septembre 1965. Hermann, Paris, p. 153.

Cosslett, V. E., Thomas, R. N., 1964a. Multiple scattering of 5 - 30 keV electrons in evaporated metal films i: Total transmission and angular distribution. Brit. J. Appl. Phys. 15, 883.

Cosslett, V. E., Thomas, R. N., 1964b. The plural scattering of 20 keV electrons. Brit. J. Appl. Phys. 15, 235.

Cosslett, V. E., Thomas, R. N., 1965. Multiple scattering of 5 - 30 keV electrons in evaporated metal films iii: Backscattering and absorption. Brit. J. Appl. Phys. 16, 779.

Crowther, J. A., 1910. On the scattering of homogeneous β-rays and the number of electrons in the atom. Proc. Royal Soc. A 84, 226.

Dees, B. C., Hamermesh, B., 1943. The small angle scattering of electrons by aluminum. Phys. Rev. 63, 297.

Draper, N. R., Smith, H., 1998. Applied Regression Analysis, 3rd Edition. Wiley, Hoboken, New Jersey.

Drescher, H., Reimer, L., Seidel, H., 1970. Rückstreukoeffizient und Sekundärelektronen-Ausbeute von 10-100 keV-Elektronen und Beziehungen zur Raster-Elektronenmikroskopie. Z. Angew. Phys. 29, 331.

Eadie, W. T., Drijard, D., James, F. E., Roos, M., Sadoulet, B., 1971. Statistical Methods in Experimental Physics. North Holland, Amsterdam, Holland.

Fano, U., 1963. Penetration of protons, alpha particles, and mesons. Ann. Rev. Nucl. Sci. 13, 1.

Fernández-Varea, J. M., Jahnke, V., Maidana, N. L., Malafronte, A. A., Vanin, V. R., 2014. Cross sections of K-shell ionization by electron impact, measured from threshold to 100 keV, for Au and Bi. J. Phys. B: At. Mol. Opt. Phys. 47, 155201.

Fernández-Varea, J. M., Mayol, R., Baró, J., Salvat, F., 1993. On the theory and simulation of multiple elastic scattering of electrons. Nucl. Instrum. Methods Phys. Res. B 73, 447.

Fernández-Varea, J. M., Salvat, F., Dingfelder, M., Liljequist, D., 2005. A relativistic optical-data model for inelastic scattering of electrons and positrons in condensed matter. Nucl. Instrum. Methods Phys. Res. B 229, 187.

Furness, J. B., McCarthy, I. E., 1973. Semiphenomenological optical model for electron scattering on atoms. J. Phys. B: At. Mol. Opt. Phys. 6, 2280.

García-Alvarez, J. A., Fernández-Varea, J. M., Vanin, V. R., Maidana, N. L., 2018. Measurement of doubly differential electron bremsstrahlung cross sections at the end point (tip) for C, Al, Te, Ta and Au. J. Phys. B: At. Mol. Opt. Phys. 51, 225003.

Glass, F. M., Courtney, C. C., Kennedy, E. J., Wilson, H. N., 1967. A new approach to direct current integration. IEEE Trans. Nucl. Sci. 14, 143.

Goudsmit, S., Saunderson, J. L., 1940a. Multiple scattering of electrons. Phys. Rev. 57, 24.

Goudsmit, S., Saunderson, J. L., 1940b. Multiple scattering of electrons. II. Phys. Rev. 58, 36.

Haque, A. K. F., Uddin, M. A., Jakubassa-Amundsen, D. H., Saha, B. C., 2018. Comparative study of eV to GeV electrons and positrons scattering elastically from neutral atoms. J. Phys. B: At. Mol. Opt. Phys. 51, 175202.

Ito, R., Tabata, T., 1970. Analytic expression for Molière integral angular distribution. Abstracts, Spring Divisional Meeting of the Physical Society of Japan 5, 164.

Jablonski, A., Salvat, F., Powell, C. J., Lee, A. Y., 2016. NIST Electron Elastic-Scattering Cross-Section Database Version 4.0, NIST Standard Reference Database Number 64, National Institute of Standards and Technology, Gaithersburg MD, 20899.
URL https://srdata.nist.gov/srd64/

Joy, D. C., 1995. A database on electron-solid interactions. Scanning 17, 270.

Kadri, O., Ivanchenko, V., Gharbi, F., Trabelsi, A., 2009. Incorporation of the Goudsmit–Saunderson electron transport theory in the Geant4 Monte Carlo code. Nucl. Instrum. Methods Phys. Res. B 267, 3624.

Kawrakow, I., Bielajew, A. F., 1998. On the condensed history technique for electron transport. Nucl. Instr. Methods Phys. Res. B 142, 253.

Kessler, J., Weichert, N., 1968. The influence of screening on Mott scattering by mercury atoms. Z. Physik 212, 48.

Kissel, L., Quarles, C. A., Pratt, R. H., 1983. Shape functions for atomic-field bremsstrahlung from electrons of kinetic energy 1–500 keV on selected neutral atoms $1 \leq Z \leq 92$. At. Data Nucl. Data Tables 28, 381.

Lewis, H. W., 1950. Multiple scattering in an infinite medium. Phys. Rev. 78, 526.

L'Hoir, A., 1984. Study of the asymmetrical response of silicon surface barrier detectors to MeV light ions. Application to the precise analysis of light ions energy spectra I. Helium ions. Nucl. Instr. Meth. 223, 336.

Liljequist, D., 1983. A simple calculation of inelastic mean free path and stopping power for 50 eV–50 keV electrons in solids. J. Phys. D: Appl. Phys. 16, 1567.

Llovet, X., Salvat, F., Bote, D., Salvat-Pujol, F., Jablonski, A., Powell, C. J., 2014. NIST Database of Cross Sections for Inner-Shell Ionization by Electron or Positron Impact, Version 1.0, NIST Standard Reference Database

Number 164, National Institute of Standards and Technology, Gaithersburg MD, 20899.
URL http://dx.doi.org/10.18434/T4N881

Malafronte, A. A., Petri, A. R., Gonçalves, J. A. C., Barros, S. F., Bueno, C. C., Maidana, N. L., Mangiarotti, A., Martins, M. N., Quivy, A. A., Vanin, V. R., 2021. A low-cost small-size commercial PIN photodiode: I. Electrical characterisation and low-energy photon spectrometry. Radiat. Phys. Chem. 179, 109103.

Mangiarotti, A., Lauth, W., Jakubassa-Amundsen, D. H., Klag, P., Malafronte, A. A., Martins, M. N., Nielsen, C., Uggerhøj, U., 2021a. Spectral distribution and Coulomb correction for nuclear bremsstrahlung induced by heavy targets. Phys. Lett. B 815, 136113.

Mangiarotti, A., Petri, A. R., Malafronte, A. A., Gonçalves, J. A. C., Barros, S. F., Bueno, C. C., Fernández-Varea, J. M., Maidana, N. L., Martins, M. N., Vanin, V. R., 2021b. A low-cost small-size commercial PIN photodiode: II. comparison of measurements with monoenergetic electrons to analytical expressions and Monte Carlo simulations. Radiat. Phys. Chem. 182, 109102.

Martins, M. N., Malafronte, A. A., Mangiarotti, A., Petri, A. R., Fernández-Varea, J. M., Maidana, N. L., Barros, S. F., Vanin, V. R., 2022. A setup for integral measurements of multiple scattering by 10- to 100-keV electrons. Radiat. Phys. Chem. 200, 110381.

Marton, L., Simpson, J. A., Fowler, H. A., Swanson, N., 1962. Plural scattering of 20-keV electrons in aluminum. Phys. Rev. 126, 182.

Molière, G., 1947. Therorie der Streuung schneller geladener Teilchen I. Einzelstreuung am abgeschirmten Coulomb-Feld. Z. Naturforsch. 2a, 133.

Negreanu, C., Llovet, X., Chawla, R., Salvat, F., 2005. Calculation of multiple-scattering angular distributions of electrons and positrons. Radiat. Phys. Chem. 74, 264.

Neubert, G., Rogaschewski, S., 1980. Backscattering coefficient measurements of 15 to 60 keV electrons for solids at various angles of incidence. Phys. Stat. Sol.(a) 59, 35.

Ning, X., Papiez, L., Sandison, G., 1995. Compound-Poisson-process method for the multiple scattering of charged particles. Phys. Rev. E 52, 5621.

Salvat, F., 2015. The PENELOPE code system. Specific features and recent improvements. Annals of Nuclear Energy 82, 98.

Salvat, F., 2019. PENELOPE-2018, A Code System for Monte Carlo Simulation of Electron and Photon Transport. OECD Nuclear Energy Agency, Workshop Proceedings, Barcelona, Spain, 28 January – 1 February.

Salvat, F., Jablonski, A., Powell, C. J., 2005. ELSEPA – Dirac partial-wave calculation of elastic scattering of electrons and positrons by atoms, positive ions and molecules. Comput. Phys. Commun. 165, 157.

Santos, O. C. B., Vanin, V. R., Maidana, N. L., Martins, M. N., Tabacniks, M. H., Rodrigues, C. L., Silva, T. F., Santos, A. D., Barros, S. F., García-Alvarez, J. A., Koskinas, M. F., Fernández-Varea, J. M., Pindzola, M. S., 2019. Experimental and theoretical cross sections for K-shell ionization of $_{52}$Te, $_{73}$Ta, and $_{83}$Bi by electrons with energies up to 100 keV. Phys. Rev. A 100, 022703.

Seltzer, S. M., Berger, M. J., 1986. Bremsstrahlung energy spectra from electrons with kinetic energy 1 keV–10 GeV incident on screened nuclei and orbital electrons of neutral atoms with Z = 1–100. At. Data Nucl. Data Tables 35, 345.

Sempau, J., Acosta, E., Baró, J., Fernández-Varea, J. M., Salvat, F., 1997. An algorithm for Monte Carlo simulation of coupled electron-photon transport. Nucl. Instrum. Methods Phys. Res. B 132, 377.

Sempau, J., Fernández-Varea, J. M., Acosta, E., Salvat, F., 2003. Experimental benchmarks of the Monte Carlo code PENELOPE. Nucl. Instrum. Methods Phys. Res. B 207, 107.

Shimizu, R., Ze-Jun, D., 1992. Monte Carlo modelling of electron–solid interactions. Rep. Prog. Phys. 55, 487.

Silva, T. F., Rodrigues, C. L., Mayer, M., Moro, M. V., Trindade, G. F., Aguirre, F. R., Added, N., Rizzutto, M. A., Tabacniks, M. H., 2016. MultiSIMNRA: A computational tool for self-consistent ion beam analysis using SIMNRA. Nucl. Instrum. Methods Phys. Res. B 371, 86.

Sternheimer, R. M., 1952. The density effect for the ionization loss in various materials. Phys. Rev. 88, 851.

Sternheimer, R. M., 1953. Erratum: The density effect for the ionization loss in various materials. Phys. Rev. 89, 1309.

Swanson, N., Powell, C. J., 1966. Inelastic scattering cross sections for 20-keV electrons in Al, Be, and Polystyrene. Phys. Rev. 145, 195.

Tabata, T., Andreo, P., Shinoda, K., 1999. Fractional energies of backscattered electrons and photon yields by electrons. Radiat. Phys. Chem. 54, 11.

Thomson, J. J., 1910. On the scattering of rapidly moving electrified particles. Proc. Camb. Phil. Soc. 15, 65.

Vanin, V. R., Maidana, N. L., Mangiarotti, A., Lima, R. R., Malafronte, A. A., Barros, S. F., Martins, M. N., 2019. The 10 – 100 keV beam line of the São Paulo Microtron electron accelerator. Radiat. Phys. Chem. 154, 26.